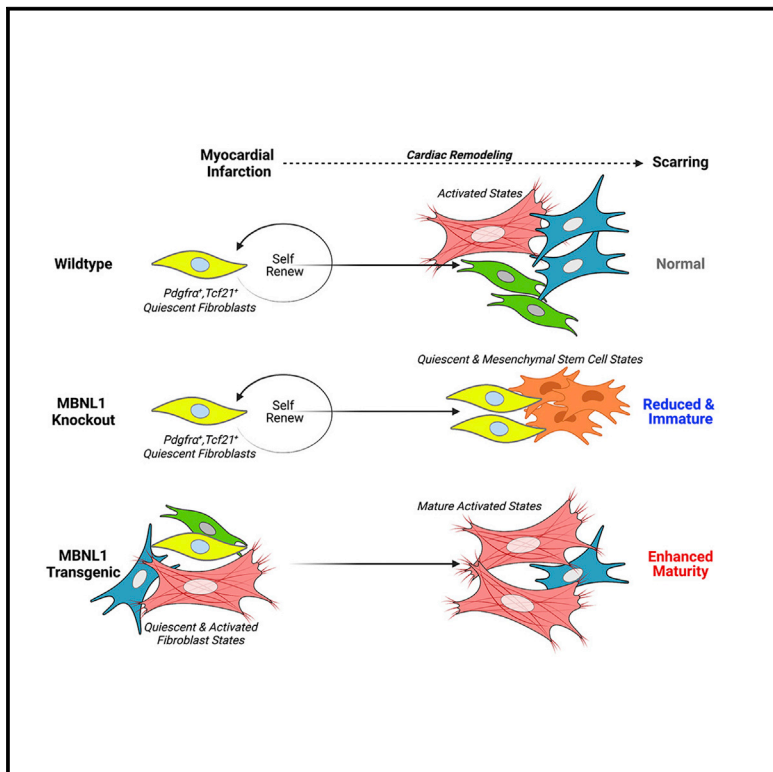


MBNL1 drives dynamic transitions between fibroblasts and myofibroblasts in cardiac wound healing

Graphical abstract



Authors

Darrian Bugg, Logan R.J. Bailey,
Ross C. Bretherton, ...,
Cole A. DeForest,
April Stempien-Otero, Jennifer Davis

Correspondence

jendavis@uw.edu

In brief

Bugg and colleagues demonstrate that following myocardial infarction, MBNL1 expression regulates cardiac fibroblast proliferation as well as the transition to and maintenance of an activated myofibroblastic state, which is associated with altered production and maturation of fibrotic scarring and cardiac muscle remodeling.

Highlights

- MBNL1 regulation of cardiac fibroblast fate modulates scar formation and maturation
- MBNL1 regulates MI-induced cardiac fibroblast proliferation
- MBNL1 is necessary and sufficient to induce and maintain mature myofibroblast states
- MBNL1 stabilizes transcripts that underlie profibrotic fibroblast states



Article

MBNL1 drives dynamic transitions between fibroblasts and myofibroblasts in cardiac wound healing

Darrian Bugg,² Logan R.J. Bailey,⁶ Ross C. Bretherton,¹ Kylie E. Beach,² Isabella M. Reichardt,¹ Kalen Z. Robeson,¹ Anna C. Reese,² Jagadambika Gunaje,² Galina Flint,¹ Cole A. DeForest,^{1,3,4} April Stempien-Otero,⁵ and Jennifer Davis^{1,2,3,7,*}

¹Department of Bioengineering, University of Washington, Seattle, WA 98105, USA

²Department of Lab Medicine & Pathology, University of Washington, Seattle, WA 98195, USA

³Institute for Stem Cell & Regenerative Medicine, University of Washington, Seattle, WA 98109, USA

⁴Department of Chemical Engineering, University of Washington, Seattle, WA 98195, USA

⁵Division of Cardiology, University of Washington, Seattle, WA 98109, USA

⁶Molecular & Cellular Biology, University of Washington, Seattle, WA 98195, USA

⁷Lead contact

*Correspondence: jendavis@uw.edu

<https://doi.org/10.1016/j.stem.2022.01.012>

SUMMARY

Dynamic fibroblast to myofibroblast state transitions underlie the heart's fibrotic response. Because transcriptome maturation by muscleblind-like 1 (MBNL1) promotes differentiated cell states, this study investigated whether tactical control of MBNL1 activity could alter myofibroblast activity and fibrotic outcomes. In healthy mice, cardiac fibroblast-specific overexpression of MBNL1 transitioned the fibroblast transcriptome to that of a myofibroblast and after injury promoted myocyte remodeling and scar maturation. Both fibroblast- and myofibroblast-specific loss of MBNL1 limited scar production and stabilization, which was ascribed to negligible myofibroblast activity. The combination of MBNL1 deletion and injury caused quiescent fibroblasts to expand and adopt features of cardiac mesenchymal stem cells, whereas transgenic MBNL1 expression blocked fibroblast proliferation and drove the population into a mature myofibroblast state. These data suggest MBNL1 is a post-transcriptional switch, controlling fibroblast state plasticity during cardiac wound healing.

INTRODUCTION

Central to heart disease is the replacement of healthy muscle with fibrotic scar tissue. While scarring prevents cardiac rupture following myocardial infarction (MI), it also causes hemodynamic dysfunction and arrhythmias that result in cardiac failure (Savarese and Lund, 2017). Scarring results from dynamic state changes in resident cardiac fibroblasts of the *Tcf21* and *Pdfgrα* lineages that respond to injury by proliferating and then transitioning into myofibroblast cells, defined by the expression of periostin (*Postn*), α-smooth muscle actin (αSMA), and the fibrotic extracellular matrix (ECM) (Davis and Molkentin, 2014). Lineage reporter studies suggest that myofibroblastic states are unstable and reversible, following exposure to pro-fibrotic stimuli by yet unresolved molecular mechanisms (Kanisicak et al., 2016).

An understudied control point for these state transitions is transcriptome maturation, which is mediated by RNA-binding proteins such as muscleblind-like 1 (MBNL1). MBNL1 modulates transcriptomes by stabilizing, splicing, polyadenylating, and localizing their target mRNAs (Batra et al., 2014; Pascual et al., 2006; Wang et al., 2012). Dysfunctional MBNL1 causes myotonic dystrophy as well as defective erythrocyte and myofibroblast

development, which has recently been linked to dysfunctional wound healing (Cheng et al., 2014; Davis et al., 2015). Indeed, global MBNL1 knockout mice have decreased myofibroblast density and fibrotic scarring following injury (Davis et al., 2015). During the transition of fibroblasts into myofibroblasts, transcripts such as serum response factor (SRF) and calcineurin (CnA), which are required for this process, are stabilized or alternatively spliced by MBNL1. While together these data suggest that MBNL1 plays an essential role in driving profibrotic states and fibrosis in the heart, this has yet to be definitively proven *in vivo*. Hence, this study tested the following hypothesis: MBNL1 post-transcriptionally regulates cardiac fibroblastic states underlying fibrotic and myocardial remodeling following injury.

MBNL1 expression was upregulated in *Postn* lineage-traced myofibroblasts after MI and in failing human cardiac fibroblasts. At baseline, cardiac fibroblast-specific expression of MBNL1 induced a mature myofibroblastic transcriptional identity, which in turn accelerated scar stabilization and maladaptive dilated remodeling with MI. Despite this fate transition, fibrotic scarring was restrained due to an MBNL1-dependent impairment of cardiac fibroblast self-renewal. During the injury response, MBNL1



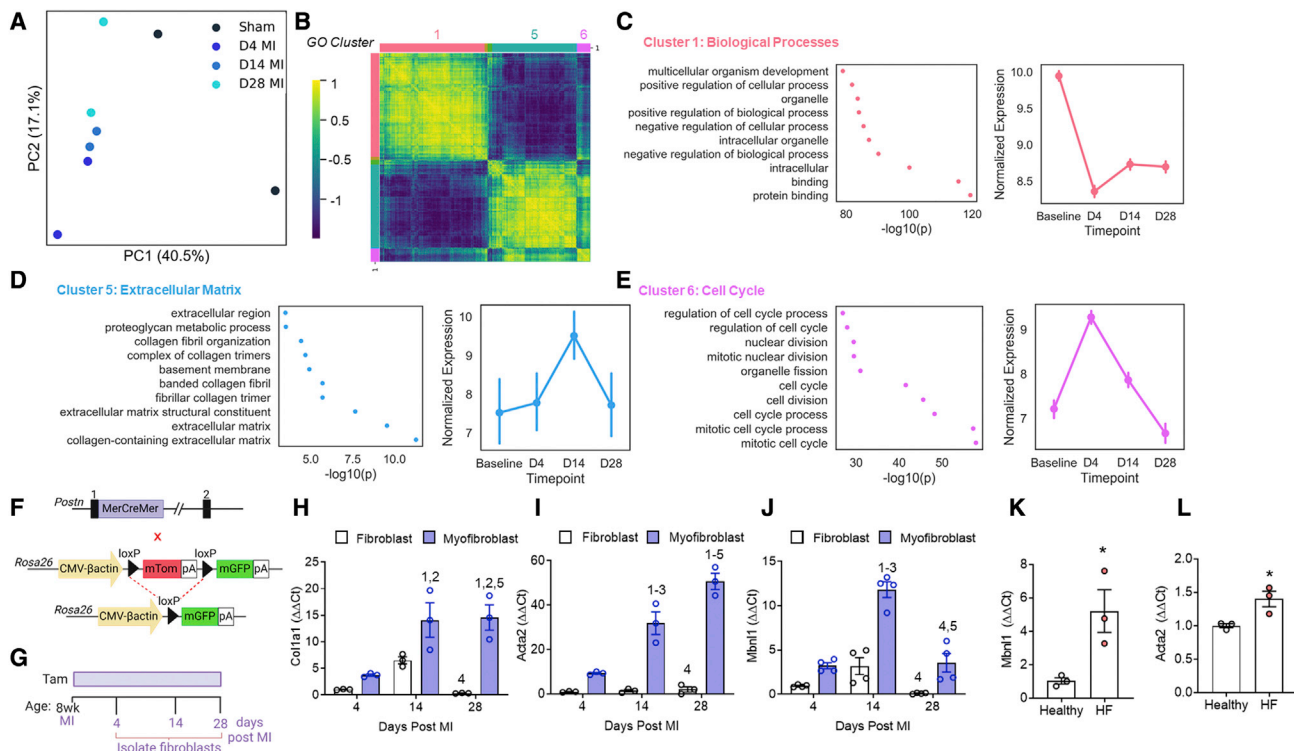


Figure 1. MBNL1 expression coincides with MI-induced myofibroblast formation

(A) PCA of cardiac fibroblast transcriptomes from sham and MI hearts at 4, 14, and 28 days.
(B) Pairwise correlation heatmap of differentially expressed genes between time points and color coded by GO clustering: 1 (salmon) = biological processes, 5 (light blue) = ECM, and 6 (pink) = cell cycle.

(C–E) GO clustering (left) and mean expression \pm 95% CI of genes within each cluster across infarct repair (right).

(F) Breeding scheme used to derive the myofibroblast lineage reporter mice (*Postn*^{iCre}-mT/mG): (top) *Postn*^{iCre} knockin mice, (bottom) mice expressing a dual fluorescent reporter (mT/mG) from the *Rosa26* locus.

(G) Timeline of Tam dosing and experimental endpoints.

(H–J) Fold change in (H) *Col1a1*, (I) *Acta2*, and (J) *Mbnl1* gene expression in cardiac myofibroblasts and quiescent fibroblasts using the $\Delta\Delta Ct$ method. Groups are compared to day-4 fibroblasts and were normalized to 18S expression; dots represent biological replicates; n = 3–4 mice per group; bars are mean \pm SEM, ANOVA + Tukey post hoc comparisons. Numbers represent significant pairwise comparisons, p < 0.05: (1) 4-day fibroblast, (2) 4-day myofibroblast, (3) 14-day fibroblast, (4) 14-day myofibroblast, (5) 28-day fibroblast, and (6) 28-day myofibroblast.

(K and L) Fold change in (K) *Mbnl1* and (L) *Acta2* gene expression in healthy and failing human fibroblasts using the $\Delta\Delta Ct$ method. Dots are biological replicates, n = 3, bars are mean \pm SEM, unpaired t test, *p < 0.05.

was required for the induction and maintenance of all activated myofibroblastic and epicardial states, which resulted in smaller immature scars. Moreover, coupling MBNL1 deletion with MI re-deployed epicardial to mesenchymal transition (EMT) genes and expanded quiescent subtypes, especially those with a cardiac mesenchymal stem cell phenotype (Chong et al., 2011; Noseda et al., 2015; White and Chong, 2020).

RESULTS

MBNL1 is upregulated in cardiac myofibroblasts

Principal component analysis (PCA) of cardiac fibroblast transcriptomes revealed time-dependent shifts in transcriptional space following MI (Figure 1A), matching known transitions between proliferative (days 1–4), myofibroblastic (days 4–14), and matrifibrocytic (days 14–21) states during infarct repair (Daseke et al., 2020; Fu et al., 2018; Mouton et al., 2019). Most of the variance between sham and MI was in the first component, while time after injury drove shifts in the second component (Figure 1A).

The associated heatmap (Figure 1B) depicts 5,141 differentially expressed (DE) genes, where the colored bars and numbers represent Gene Ontology (GO) clusters (Raudvere et al., 2019). Genes involved in normal fibroblast function were downregulated over time (Figure 1C); those associated with the ECM were upregulated (Figure 1D), and cell cycle genes were highly expressed at day 4 but regressed thereafter (Figure 1E).

To compare gene expression profiles between quiescent and activated cardiac fibroblasts, *Postn* lineage reporter mice (*Postn*^{iCre}-mT/mG), generated by crossing mice containing a tamoxifen (Tam)-inducible Cre recombinase in the *Postn* locus (*Postn*^{iCre}) with mice containing a membrane-targeted dual fluorescent reporter in the *Rosa26* locus (mT/mG, Figure 1F), were used to segregate both states by fluorescence-activated cell sorting (FACS) (Kanisicak et al., 2016). Tam labeling began at the time of surgery and was maintained until each endpoint (Figure 1G). *Postn*-traced fibroblasts had a significant upregulation of canonical myofibroblastic genes such as *Col1a1* and *Acta2* relative to unlabeled quiescent fibroblasts at all time points

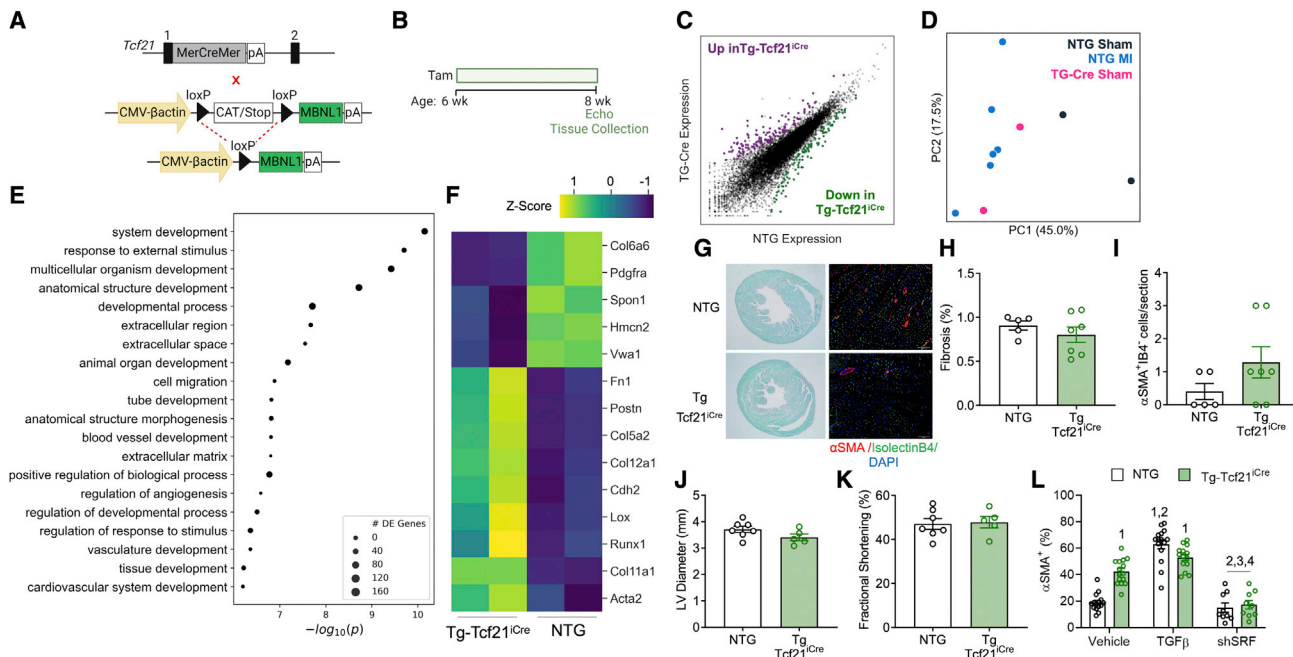


Figure 2. Cardiac fibroblast-specific MBNL1 overexpression induces a myofibroblast phenotype

- (A) Breeding scheme for generating MBNL1 Tg-Tcf21^{iCre} mice: (top) Tcf21^{iCre} mice, (bottom) conditional MBNL1 transgenic mice (Tg-Tcf21^{iCre}).
 (B) Tam dosing timeline and experimental endpoints.
 (C) Scatterplot of differentially expressed cardiac fibroblast genes. NTG = non transgenic, purple dots are significantly upregulated genes and green dots are significantly downregulated genes in Tg-Tcf21^{iCre} mice.
 (D) PCA of sham uninjured Tg-Tcf21^{iCre} as well as sham and injured NTG cardiac fibroblasts.
 (E) Functional clustering of differentially expressed cardiac fibroblast genes between Tg-Tcf21^{iCre} and NTG at baseline. Size of circle = number of DE genes per cluster.
 (F) Heatmap of the top 14 differentially expressed myofibroblast genes at baseline.
 (G) Sirius red/fast green-stained (left) and immunofluorescent imaging of myofibroblasts (right) in myocardial sections following 14 days of Tam.
 (H) Quantification of cardiac fibrosis identified in (G, left). Dots are biological replicates, bars are mean ± SEM, unpaired t tests, p = 0.3551.
 (I) Quantification of myofibroblast density from (G, right). Myofibroblasts are αSMA (red) positive and negative for the endothelial marker isolectinB4 (green). Nuclei are blue. Scale bars, 50 μm. Dots are biological replicates, Tg-Tcf21^{iCre} (n = 6), NTG (n = 5), bars are mean ± SEM, unpaired t tests, p = 0.1730.
 (J) and (K) Quantification of (J) left ventricular diastolic diameter, p = 0.0828 and (K) fractional shortening, p = 0.8372. Dots are biological replicates, Tg-Tcf21^{iCre} (n = 5), NTG (n = 7), bars represent mean ± SEM, unpaired t tests.
 (L) Quantification of the percentage of Tg-Tcf21^{iCre} and NTG cardiac fibroblasts treated with vehicle, TGFβ, or adenovirally transduced with SRF shRNA that are αSMA+. Dots are biological replicates (n = 18), bars are mean ± SEM, ANOVA statistical test with Tukey post hoc comparisons, p < 0.05: (1) NTG vehicle, (2) Tg-Cre vehicle, (3) NTG TGFβ, (4) Tg-Cre TGFβ, (5) NTG shSRF, and (6) Tg-Cre shSRF. See also Figure S1.

following MI (Figures 1H and 1I). Owing to previous work identifying MBNL1 as an activator of myofibroblastic differentiation (Davis et al., 2015), *Mbnl1* gene expression was also examined and found to be elevated in *Postn*-traced myofibroblasts at days 4 and 14 when compared with quiescent fibroblasts (Figure 1J). Furthermore, cardiac fibroblasts from failing human hearts, a tissue source rich in myofibroblasts (Farris et al., 2017; Willems et al., 1994), had a significant upregulation of *Mbnl1* and *Acta2* (Figures 1K and 1L), suggesting that MBNL1 activity is associated with myofibroblast formation in both humans and mice.

MBNL1 promotes a myofibroblast phenotype

To examine whether MBNL1 overexpression transitions cardiac fibroblasts into myofibroblasts, conditional MBNL1 transgenic (Tg) mice were crossed with a cardiac fibroblast-specific Cre driver that was engineered by knocking a Tam-inducible Cre recombinase into the *Tcf21* locus (Tcf21^{iCre}, Figure 2A, Acharya et al., 2011, 2012). Non transgenic (NTG-Tcf21^{iCre}) and Tg-

Tcf21^{iCre} littermates were administered Tam for 2 weeks (Figure 2B), and then FACS sorted cardiac fibroblasts were analyzed by RNA sequencing (RNA-seq), which identified 420 DE genes between groups (Figure 2C). Several transcripts upregulated in Tg fibroblasts and previously identified as MBNL1 targets were myofibroblast signature genes such as *Lox*, *Postn*, *Fn1*, and *Ccn4* (Figure S1A; Davis et al., 2015). PCA demonstrated that forced MBNL1 expression transitioned cardiac fibroblasts into the same transcriptional space as NTG fibroblasts from infarcted hearts (Figure 2D). Over the course of infarct repair, 2,803 transcripts were DE in NTG fibroblasts (Figure S1B). Of those, 270 transcripts were shared between Tg and infarcted NTG fibroblasts, with the greatest overlap observed at day 14, in which 10% were in common (Figure S1B). Given that days 4–14 represent the period of maximal myofibroblast differentiation (Fu et al., 2018), these data provided further evidence that MBNL1 expression is sufficient to transition the cardiac fibroblast transcriptome to that of a

myofibroblast without an injury. GO term analysis of DE genes revealed an enrichment in the ECM and cardiovascular developmental pathways (Figure 2E). Further examination of this RNA-seq data set demonstrated that several fundamental myofibroblastic transcriptional markers (*Acta2*, *Postn*, *Fn1*, *Lox*, and *Col5a2*) were among the top 25 DE genes in uninjured MBNL1 Tg-Tcf21^{iCre} fibroblasts when compared with NTGs (Figure 2F). Despite Tg fibroblasts having a profibrotic myofibroblast transcriptome (Figures 2D and 2F), no differences were identified in cardiac fibrosis (Figures 2G and 2H), α SMA⁺ myofibroblast number (Figures 2G and 2I), or cardiac structure (Figure 2J) and function (Figure 2K) when comparing groups. It was hypothesized that an additional stimulus is needed to achieve physiologic myofibroblast phenotypes. Thus, cardiac fibroblasts were isolated from Tam-treated NTG and MBNL1 Tg-Tcf21^{iCre} mice, and immunofluorescent imaging was used to quantify the number of cardiac fibroblasts with α SMA⁺ stress fibers, a physiologic marker of differentiated myofibroblasts (Figure 2L; Bretherton et al., 2020). At baseline, there was a 2-fold increase in α SMA⁺ fibroblasts in the Tg versus NTG group, suggesting that Tg fibroblasts are poised to become *bona fide* myofibroblasts. Stimulation by transforming growth factor- β (TGF β) in conjunction with the rigidity of tissue culture plastic did not additively increase α SMA⁺ fibroblast numbers in the Tg group (Figure 2L). This differed from NTGs that required TGF β to reach the same percentage of α SMA⁺ fibroblasts measured in Tgs at baseline (Figure 2L). These results imply that additional profibrotic cues—such as the stiffness—are needed to fully transform MBNL1 Tg fibroblasts to a physiologic myofibroblastic state. Previously, we demonstrated that TGF β -mediated induction of myofibroblast genes requires SRF, a transcript stabilized by MBNL1 binding to its 3' UTR (Davis et al., 2012, 2015). Acute shRNA knockdown of SRF blocked TGF β -mediated myofibroblast differentiation in both MBNL1 Tg-Tcf21^{iCre} and NTG-Tcf21^{iCre} cardiac fibroblasts, demonstrating that SRF transcriptional activity acts downstream of MBNL1.

MBNL1 blocks MI-induced cardiac fibroblast proliferation and enhances scar stability

To bring out the fibrotic phenotype, MBNL1 Tg-Tcf21^{iCre} and NTG mice were subjected to MI following 2 weeks of Tam (Figure 3A). MI significantly upregulated several collagen genes (*Col1a1*, *Col1a2*, *Col3a1*, *Col5a1*, and *Col5a2*, Figure 3B) in cardiac fibroblasts from Tg relative to NTG hearts, matching a CLIP-seq study showing that MBNL1 localizes mRNAs for secreted factors such as collagens and fibronectins (Wang et al., 2012). Immunocytochemistry with *Col3a1* and *Col5a1* antibodies was performed on Tg and NTG myocardial sections to verify these changes. No differences were observed in *Col3a1* staining, but *Col5a1* was slightly elevated in MBNL1 Tg-Tcf21^{iCre} hearts (Figures S2A–S2C). Similarly, myofibroblast density and overall fibrosis did not differ between genotypes (Figures 3C–3F). Since more mature myofibroblast fates stabilize the fibrotic ECM (Fu et al., 2018), collagen birefringence was measured in Sirius red/fast green-stained myocardial sections, which also showed no differences in the proportion of mature red versus immature green collagen fibers 2 weeks following MI (Figures 3E and 3G). Scar morphology was also analyzed by second harmonic

generation (SHG) in decellularized mouse hearts. Here, no differences in collagen fiber number, alignment, or width were detected (Figures S2D–S2F), although collagen fibers in the border zone of Tg hearts were significantly shorter (Figure 3H). The biomechanical ramifications of short collagen fibers are unclear, but in Tg mice fractional shortening dropped by 10% along with slightly more ventricular dilation (Figures 3I and 3J). Alternatively, this depressed systolic function could be a result of signaling between Tg fibroblasts and myocytes that initiate cell death or contractile dysfunction. TUNEL staining of myocytes colabeled with α Actinin showed no differences in apoptosis between genotypes (Figure 3K), but infarcted Tg myocytes had a more robust contractile function and faster relaxation when compared with NTGs (Figures S3A–S3D). Specifically, Tg myocytes produced larger and faster contractions (Figures 3L and 3M) with a more severe dilated morphology characterized by increased cell length and decreased width (Figures 3N and 3O). Because sarcomere lengths were not different between groups (Figure S3E), the severe myocyte dilation was ascribed to serial sarcomere addition, which likely drives the heightened function of Tg myocytes under unloaded conditions.

Aging MBNL1 Tg-Tcf21^{iCre} mice promotes interstitial fibrosis in the absence of injury (Davis et al., 2015), and thus additional cohorts of Tg and NTG mice were subjected to MI and examined 3 months later when the infarct scar had fully remodeled (Figure 3P). While the total area of fibrotic scarring, myofibroblast density, and myocardial remodeling were indistinguishable between genotypes (Figures S4A–S4F), scars in Tg mice were more mature, as indicated by the greater percentage of red-white collagen fibers detected by collagen birefringence imaging (Figures 3Q and 3R). This enhanced scar maturation in MBNL1 Tg-Tcf21^{iCre} mice is consistent with the increased expression of matrix maturation factors such as *Lox* and *Runx1*, which were overexpressed in Tg cardiac fibroblasts at baseline (Figure 2F). Possible explanations for the modest change in myofibroblast numbers and the amount of fibrosis after MI is that forced expression of MBNL1 limits fibroblast numbers by inducing apoptosis or inhibiting the proliferative phase of wound healing. Two days after MI, TUNEL staining of cardiac fibroblasts colabeled with PDGFR α detected no differences in the amount of fibroblast cell death between groups (Figure 3S). To measure proliferation, mice were given 5-ethyl-2'-deoxyuridine (EdU) over the 2 days following injury, and then proliferating fibroblasts were identified in myocardial sections by measuring the number of PDGFR α ⁺, EdU⁺ cells (Figures 3T and 3U). Tg mice had 20% fewer proliferating PDGFR α ⁺, EdU⁺ cardiac fibroblasts relative to NTGs (Figure 3U). Proliferation was also measured *in vitro* under differentiation conditions (Figure 3V, 2% Serum), and similar to the *in vivo* findings, Tg cardiac fibroblasts had significantly reduced proliferative capacity when compared with NTGs (Figure 3V). Moreover, RNA-seq analysis showed that positive cell cycle regulators such as *Ccnb2*, *Ccna2*, *Birc5*, and *Kif23* were all downregulated in Tg cardiac fibroblasts 4 days after MI, while cell cycle inhibitors such as *Cxcl1* and *Cdkn1a* were significantly upregulated (Figure S4G). Collectively, these data suggest that the decreased fibroblast proliferation in MBNL1 Tg-Tcf21^{iCre} mice prevented the additive effects of MBNL1 expression and injury on myofibroblast density and scarring.

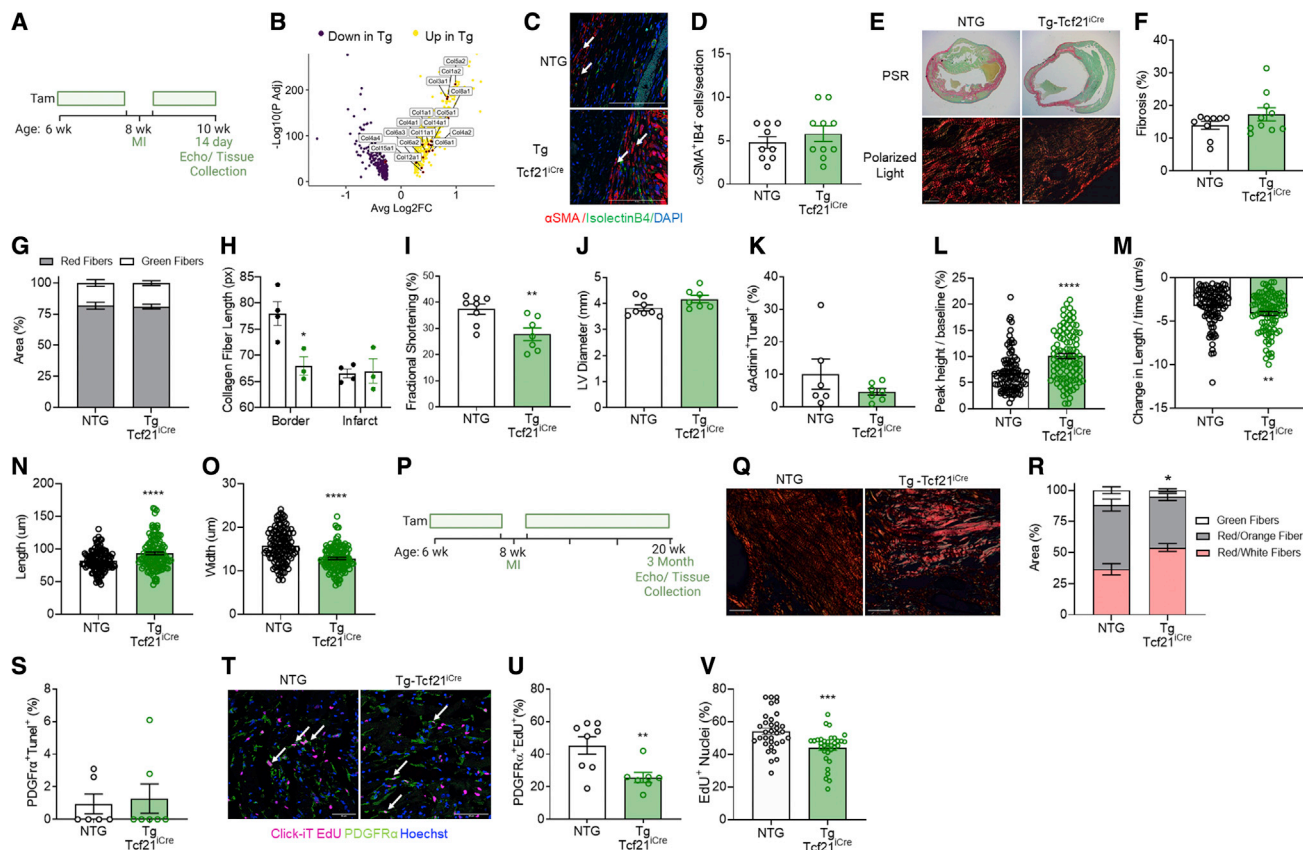


Figure 3. Overexpression of MBNL1 in cardiac fibroblasts prevents MI-dependent fibroblast proliferation

(A) Timeline of Tam dosing, MI surgery, and experimental endpoints.

(B) Volcano plot of differentially expressed collagens 7 days post MI. Yellow dots are upregulated genes and purple dots are downregulated genes in Tg-Tcf21^{iCre} cardiac fibroblasts.

(C and D) (C) Immunofluorescent imaging and (D) quantification of myofibroblasts in myocardial sections 14 days following MI. Myofibroblasts are α SMA (red) positive and negative for the endothelial marker isolectinB4 (green). Nuclei are stained blue. Arrows show α SMA⁺IB4⁻ cells. Scale bars, 50 μ m. Dots are biological replicates, Tg-Tcf21^{iCre} (n = 10), NTG (n = 9), bars are mean \pm SEM, unpaired t tests, p = 0.3791.

(E–G) (E) Brightfield (top) and 40 \times polarized light (bottom, scale bars, 20 μ m) images and (F) quantification of fibrosis and (G) collagen birefringence in Sirius red/fast green-stained myocardial sections. Dots are biological replicates, Tg-Tcf21^{iCre} (n = 10), NTG (n = 9), unpaired t tests, p < 0.05.

(H) Quantification of collagen fiber length by second harmonic generation in decellularized hearts 30 days post MI. Dots are biological replicates, Tg-Tcf21^{iCre} (n = 3), NTG (n = 4), bars are mean \pm SEM, t tests, *p < 0.05.

(I and J) Quantification of left ventricular (I) fractional shortening, **p < 0.01, and (J) diastolic diameter, p = 0.0828. Dots are biological replicates, Tg-Tcf21^{iCre} (n = 7), NTG (n = 8), bars are mean \pm SEM, unpaired t tests.

(K) Quantification of apoptotic myocytes (α Actinin⁺ Tunel⁺) as a percentage of total in cardiac sections 2 days post MI. Dots are biological replicates, Tg-Tcf21^{iCre} (n = 7), NTG (n = 6), bars are mean \pm SEM, and unpaired t tests, p = 0.2450.

(L–O) Isolated myocyte (L) fractional shortening, (M) rate of contraction, (N) length, and (O) width measured 14 days post MI. Dots are individual myocytes (30–40/mouse), Tg-Tcf21^{iCre} (n = 3), NTG (n = 3) mice, bars are mean \pm SEM, unpaired t tests, ***p < 0.0001, **p < 0.0001, *p < 0.01.

(P) Timeline of Tam dosing scheme for 3 months of recovery from MI.

(Q and R) (Q) Images and (R) quantification of collagen birefringence in Sirius red/fast green-stained myocardial sections from Tg-Tcf21^{iCre} (n = 4) and NTG (n = 4). Scale bars, 20 μ m. Bars are mean \pm SEM, unpaired t test: red/white fibers p = 0.0062, red/orange fibers p = 0.0670, green fibers p = 0.0447.

(S) Quantification of apoptotic fibroblasts (PDGFR α ⁺ Tunel⁺) as a percentage of total in cardiac sections 2 days post MI. Dots are biological replicates, Tg-Tcf21^{iCre} (n = 7), NTG (n = 6), bars are mean \pm SEM, unpaired t tests, p = 0.7797.

(T and U) (T) Immunofluorescent staining and (U) quantification of proliferating fibroblasts (PDGFR α ⁺, EdU⁺) 2 days post MI in Tg-Tcf21^{iCre} (n = 8) and NTG (n = 7) hearts. PDGFR α (green), EdU (pink), nuclei (blue), and arrows show PDGFR α ⁺, EdU⁺ fibroblasts. Scale bars, 50 μ m. Dots are biological replicates, bars are mean \pm SEM, unpaired t tests, **p < 0.01.

(V) Quantification of *in vitro* fibroblast proliferation in low serum. Dots are technical replicates, Tg Tcf21^{iCre} (n = 11), NTG (n = 11). Bars are mean \pm SEM, unpaired t test, ***p < 0.001. See also Figures S2, S3, and S4.

Loss of MBNL1 blocks myofibroblast differentiation, fibrosis, and scar maturation

Conditional MBNL1 knockouts (MBNL1^{F1/F1}) were crossed with Tcf21^{iCre} mice to examine the requirement for MBNL1 in cardiac

fibroblast to myofibroblast state transitions (Figure 4A). Western blotting of TGF β -treated cardiac fibroblasts shows the robust deletion of MBNL1 with Tam induction in MBNL1^{F1/F1}-Tcf21^{iCre} mice (F1-Tcf21^{iCre}) when compared with their MBNL1^{F1/F1}

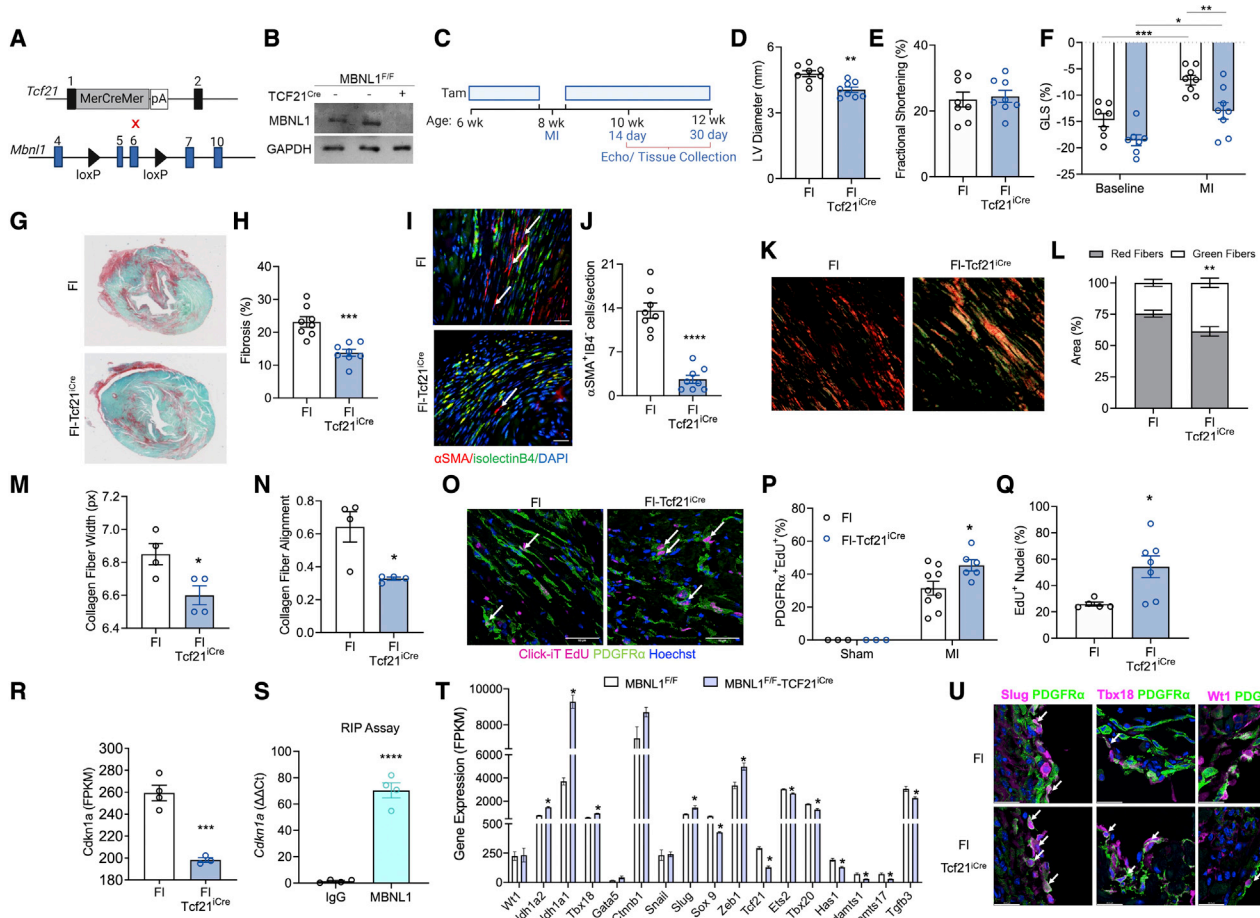


Figure 4. MBNL1 is required for cardiac fibroblast state transitions and fibrotic scarring

(A) Breeding scheme for cardiac fibroblast-specific MBNL1 knockout mice ($MBNL1^{Fl/Fl}$ - $Tcf21^{iCre}$): (top) Tg- $Tcf21^{iCre}$ mice crossed with (bottom) conditional $Mbnl1$ knockout mice ($MBNL1^{Fl/Fl}$ - $Tcf21^{iCre}$).

(B) Western blot of MBNL1 expression from Tam-treated $MBNL1^{Fl/Fl}$ - $Tcf21^{iCre}$ and $MBNL1^{Fl/Fl}$ cardiac fibroblasts + recombinant TGF β . Glyceraldehyde-3-Phosphate Dehydrogenase (GAPDH) was the loading control.

(C) Timeline of Tam dosing, MI, and experimental endpoints.

(D–F) Quantification of left ventricular (D) diastolic diameter, ** $p < 0.01$, (E) fractional shortening, $p = 0.7499$, and (F) global longitudinal strain (GLS) * $p < 0.05$, ** $p < 0.01$, *** $p < 0.001$, at 14 days post MI. Dots are biological replicates, $MBNL1^{Fl/Fl}$ - $Tcf21^{iCre}$ ($n = 8$), $MBNL1^{Fl/Fl}$ ($n = 8$), bars are mean \pm SEM, unpaired t tests for (D and E) and two-way ANOVA for (F).

(G and H) Images and (H) quantification of Sirius red/fast green-stained myocardial sections. Dots are biological replicates, bars are mean \pm SEM, unpaired t tests, *** $p < 0.001$.

(I and J) (I) Immunofluorescent imaging and (J) quantification of myofibroblasts in the border zone of myocardial sections 14 days post MI. Myofibroblasts are α SMA (red) positive and negative for the endothelial marker isolectin B4 (green). Nuclei are blue. Arrows show α SMA $^+$ IB4 $^-$ cells. Scale bars, 50 μ m. Dots are biological replicates, $MBNL1^{Fl/Fl}$ - $Tcf21^{iCre}$ ($n = 8$), $MBNL1^{Fl/Fl}$ ($n = 8$), bars are mean \pm SEM, unpaired t tests, *** $p < 0.0001$.

(K and L) (K) Images and (L) quantification of collagen birefringence in myocardial sections from $MBNL1^{Fl/Fl}$ - $Tcf21^{iCre}$ ($n = 4$) and $MBNL1^{Fl/Fl}$ ($n = 4$) mice. Scale bars, 20 μ m. Bars are mean \pm SEM, unpaired t tests, ** $p < 0.01$.

(M and N) Quantification of (M) collagen fiber width and (N) alignment from second harmonic generation decellularized hearts 30 days post MI. Dots are biological replicates, $MBNL1^{Fl/Fl}$ - $Tcf21^{iCre}$ ($n = 4$), $MBNL1^{Fl/Fl}$ ($n = 4$), bars are mean \pm SEM, unpaired t tests, * $p < 0.05$.

(O and P) (O) Immunofluorescent imaging and (P) quantification of proliferating fibroblasts ($PDGFR\alpha^+$, EdU^+) in myocardial sections from $MBNL1^{Fl/Fl}$ - $Tcf21^{iCre}$ (Sham $n = 3$, MI $n = 6$) and $MBNL1^{Fl/Fl}$ (Sham $n = 3$, MI $n = 9$) mice 2 days post MI. $PDGFR\alpha^+$ (green), EdU^+ (pink), nuclei (blue). Arrows show $PDGFR\alpha^+$, EdU^+ cells. Scale bars, 50 μ m. Dots are biological replicates, bars are mean \pm SEM, unpaired t tests, * $p < 0.05$.

(Q) Quantification of *in vitro* cardiac fibroblast proliferation in low serum. Dots are biological replicates ($n = 7$ per genotype), bars are mean \pm SEM, unpaired t test, * $p < 0.05$.

(R) Gene expression (FPKM, fragments per kilobase of transcript) of *Cdkn1a* in $MBNL1^{Fl/Fl}$ - $Tcf21^{iCre}$ ($n = 3$) and $MBNL1^{Fl/Fl}$ ($n = 4$) cardiac fibroblasts 4 days post MI. Dots are biological replicates, bars are mean \pm SEM, unpaired t test, *** $p < 0.001$.

(S) Expression of *Cdkn1a* transcripts immunoprecipitated by MBNL1 in cardiac fibroblasts. Dots are biological replicates, bars are mean \pm SEM, unpaired t test, *** $p < 0.0001$.

(legend continued on next page)

littermates (Figure 4B). At baseline, cardiac fibroblast-specific deletion of MBNL1 did not affect heart function (data not shown), but after MI, Fl-Tcf21^{iCre} mice were protected from ventricular dilation (Figures 4C and 4D). Neither genotype exhibited differences in fractional shortening by echocardiography (Figure 4E), but speckle tracking of global longitudinal strain (GLS) revealed that Fl-Tcf21^{iCre} mice had improved systolic function (Figure 4F). Fibrosis and myofibroblast density were reduced by 40% in Fl-Tcf21^{iCre} versus MBNL1^{F/F} controls, demonstrating that MBNL1 is required for myofibroblast formation and fibrosis (Figures 4G–4J). *Col3a1* and *Col5a1* were also examined in serial sections, and although no differences were detected in *Col3a1*, *Col5a1* was significantly downregulated in Fl-Tcf21^{iCre} hearts (Figures S5A–S5C). Collagen fiber maturity was also examined by imaging collagen birefringence, which showed that the Fl-Tcf21^{iCre} ECM had a great proportion of immature green collagen fibers relative to MBNL1^{F/F} (Figures 4K and 4L). Collagen fiber width and alignment were also decreased in Fl-Tcf21^{iCre} hearts (Figures 4M and 4N), which is indicative of an immature and unstable scar (Holmes et al., 1997; Quinn et al., 2016; Richardson et al., 2015). These data coincide with downregulated ECM maturation genes, such as *Postn*, *Col1a1*, *Col1a2*, *Comp*, *Loxl3*, *Lox*, and *Runx1* in Fl-Tcf21^{iCre} cardiac fibroblasts (Figure S5D). Surprisingly, there were no differences in cardiac rupture between genotypes. Fl-Tcf21^{iCre} cardiac fibroblasts were examined *in vitro* to ascertain whether fibroblast differentiation defects underlie the poor production and maturation of fibrotic scar tissue. TGFβ treatment caused 73% ± 3.46% of MBNL1^{F/F} cardiac fibroblasts to develop αSMA⁺ stress fibers, whereas Fl-Tcf21^{iCre} fibroblasts were refractory to that differentiation cue (Figures S5E and S5F). Given that MBNL1 stabilizes SRF (Davis et al., 2015), it was reasoned that expressing a stabilized SRF cDNA should rescue TGFβ-mediated myofibroblast differentiation in Fl-Tcf21^{iCre} cardiac fibroblasts. Hence, MBNL1^{F/F} and Fl-Tcf21^{iCre} cardiac fibroblasts were adenovirally transduced with SRF (AdSRF), which restored the ability of Fl-Tcf21^{iCre} fibroblasts to transition into myofibroblasts with TGFβ (Figures S5E and S5F). Similar results were achieved with adenoviral re-expression of MBNL1 (AdMBNL1, Figures S5E and S5F), indicating that these cells are still competent to undergo programmed state transitions provided MBNL1 and its downstream regulatory targets are functional. Another hallmark of myofibroblasts is contractile function, which is needed to close wounds and is measured using collagen gel contraction assays (Davis and Molkentin, 2014). Here, MBNL1^{F/F} or Fl-Tcf21^{iCre} cardiac fibroblasts were seeded in collagen gels, and the gel area was measured to estimate cell contractility. 48 h after seeding, MBNL1^{F/F} gels contracted to 80% of the original size versus 96% in Fl-Tcf21^{iCre} gels (Figures S5G and S5H). TGFβ treatment elicited the extensive contraction of MBNL1^{F/F} gels, but not in those containing Fl-Tcf21^{iCre} fibroblasts (Figures S5G and S5H). Again, AdMBNL1 or the expression of a constitutively active variant of calcineurin (AdΔCnA) that is alternatively

spliced by MBNL1 (Davis et al., 2012, 2015), partially restored contraction in the Fl-Tcf21^{iCre} cardiac fibroblasts, providing functional evidence of MBNL1's essential role in myofibroblast state transitions (Figures S5G and S5H).

Infarcted MBNL1-null fibroblasts redeploy developmental signals and self-renew

The lack of myofibroblasts in Fl-Tcf21^{iCre} myocardial sections following MI could be due to both proliferation and differentiation defects, as MBNL1 overexpression was found to block MI-induced cardiac fibroblast proliferation (Figures 3T–3V). MBNL1^{F/F} and Fl-Tcf21^{iCre} mice were subjected to MI, and EdU was used to label proliferating cells for 2 days following injury. In Fl-Tcf21^{iCre} hearts, 45% of the total PDGFRα⁺ fibroblast population was EdU⁺ versus 31% in the MBNL1^{F/F} controls (Figures 4O and 4P). This result was consistent with heightened *in vitro* proliferation capacity, increased expression of positive cell cycle regulators *Cdk6* and *Ccnd1*, and decreased expression of potent cell cycle inhibitors *Cdkn1a* and *Cdkn2aip* in Fl-Tcf21^{iCre} cardiac fibroblasts 4 days after MI (Figures 4Q, 4R, and S5I–S5K). Because there was antithetical expression of *Cdkn1a* in MBNL1 Tg-Tcf21^{iCre} mice (Figure S4G), RNA immunoprecipitation was used to confirm that MBNL1 binds *Cdkn1a* in adult cardiac fibroblasts (Figure 4S), matching previous results obtained in mouse embryonic fibroblasts (MEFs) with MBNL1 overexpression (Davis et al., 2015).

Since heightened proliferation is often associated with dedifferentiation (Daseke et al., 2020; Fu et al., 2018; Mouton et al., 2019), RNA-seq analysis of cardiac fibroblast transcriptomes was used to examine whether MBNL1 deletion facilitates dedifferentiation in response to injury. Relative to MBNL1^{F/F}, Fl-Tcf21^{iCre} fibroblasts had downregulated cardiac fibroblast specification transcripts, including: *Sox9*, *Tcf21*, *Ets2*, *Tbx20*, *Tgfβ3*, *Adamts1*, and *17* (Figures 4T and 4U). Yet other positive drivers of EMT, such as *Zeb1* and *Slug* as well as epicardial development genes *Aldh1a2*, *Aldh1a1*, and *Tbx18*, were also upregulated in Fl-Tcf21^{iCre} cardiac fibroblasts (von Gise and Pu, 2012; von Gise et al., 2011; Huang et al., 2012; Xavier-Neto et al., 2000). Indeed, a greater number of PDGFRα⁺ cardiac fibroblasts colocalized with *Slug* and *Tbx18* but not with WT1 in Fl-Tcf21^{iCre} myocardial sections (Figures 4T and 4U). The combination of re-expression of early fibroblast developmental genes and enhanced proliferation suggests that MBNL1-null cardiac fibroblasts are more plastic than wild-type and that they may promote repair, as similar changes in fibroblast gene expression occur during cardiac regeneration (Cao and Poss, 2018).

MBNL1 restricts cardiac fibroblast plasticity and population diversity

The altered expression of EMT regulatory genes did not conclusively establish whether these signals were due to MBNL1's role in fibroblast fate or the reactivation of the epicardium. To examine this question, single cell RNA-seq (scRNA-seq) was performed on cardiac fibroblasts isolated from sham and infarcted hearts of

(T) Expression of EMT and cardiac fibroblast specification genes in MBNL1^{F/F} Tcf21^{iCre} (n = 4) and MBNL1^{F/F} (n = 6) cardiac fibroblasts 4 days post MI. Bars are mean ± SEM, p < 0.05.

(U) Immunofluorescent imaging of epicardial markers SLUG (left, pink), TBX18 (middle, pink), and WT1 (right, pink) colocalized with PGFRα⁺ (green) in myocardial sections 7 days post MI. Scale bars, 24.2 μm. See also Figure S5.

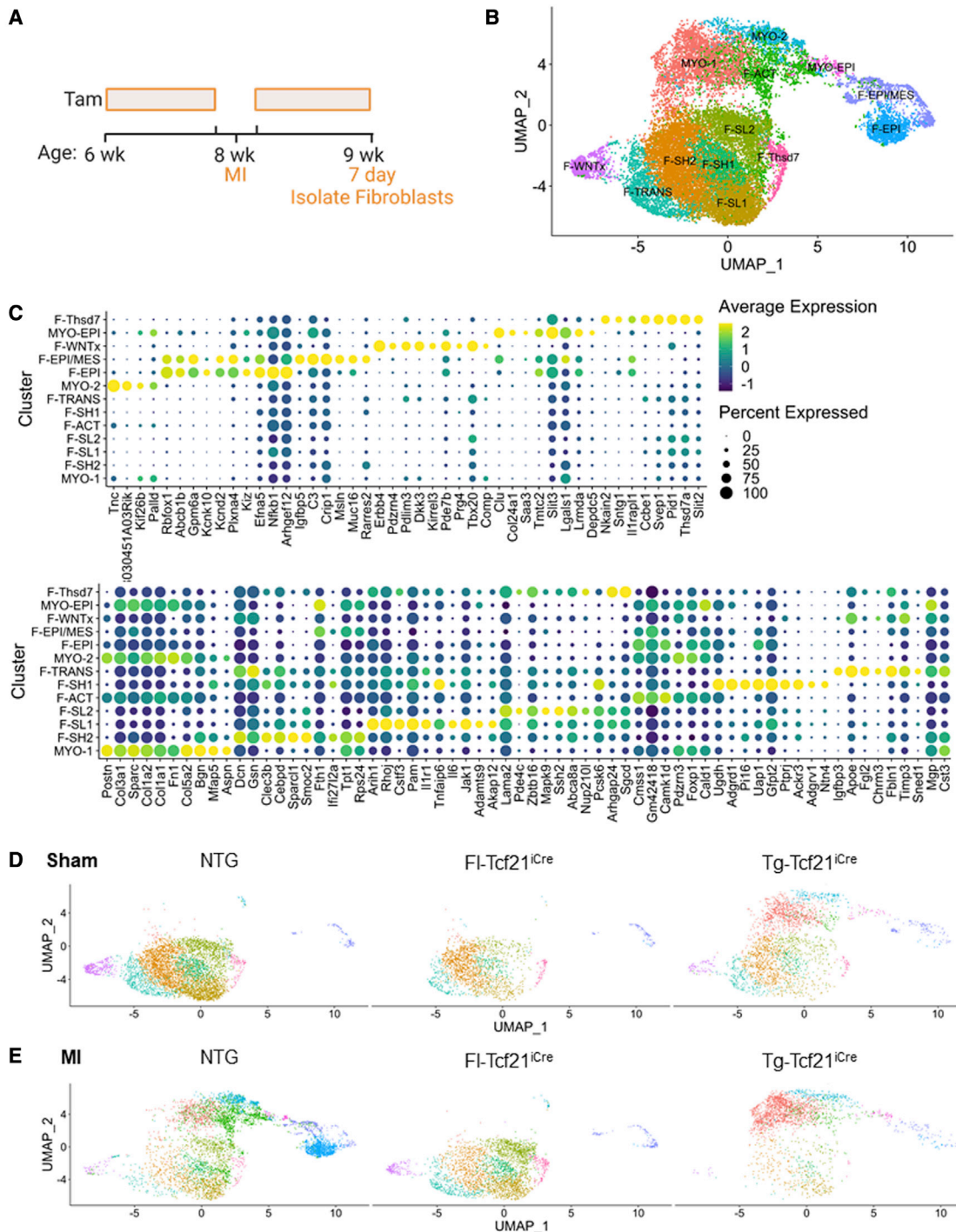


Figure 5. scRNA-seq reveals that MBNL1 functions as a post-transcriptional switch between fibroblast and myofibroblast states

(A) Timeline of MI injury, Tam dosing, and experimental endpoints.

(B) UMAP dimensionality reduction plot of all 20,814 sequenced cardiac fibroblasts independent of genotypes/experimental condition and clustered by differential gene expression. Each colored dot represents a unique cell state.

(C) Dot plot of the top 10 significantly expressed genes defining each cluster.

(D and E) UMAP dimensionality reduction plots divided by experimental condition (D) Sham and (E) MI and genotype: NTG/Sham ($n = 2$), NTG/MI ($n = 2$), MBNL1^{F/F}-Tcf21^{iCre}/Sham ($n = 2$), MBNL1^{F/F}-Tcf21^{iCre}/MI ($n = 2$), and MBNL1Tg-Tcf21^{iCre}/Sham ($n = 2$), MBNL1Tg-Tcf21^{iCre}/MI ($n = 2$). See also Figure S6.

NTG, Fl-Tcf21^{iCre} and Tg mice (Figure 5A). Transcriptional profiles of a total of 20,814 cells were captured after quality control filtering. Thirteen different fibroblastic substates were identified by hierarchical clustering based on differential gene expression, with each of the clusters expressing the canonical fibroblast markers *Col1a1* and *Col3a1*, albeit with varying levels of expression (Figure 5B, S6A, and S6B). Each cluster was labeled using preestablished nomenclature (Farbahi et al., 2019; Skelly et al., 2018), and two large clusters (quiescent and myofibroblast) were identified. Within the quiescent cluster there were nine substates (F-SH1-2, F-SL1-2, F-TRANS, F-EPI, F-EPI/MES, F-WNTx, F-THSD7), with the myofibroblast cluster having four (MYO-1-2, F-ACT, MYO-EPI, Figures 5B and 5C). These larger clusters were defined by the enhanced expression of quiescent markers *Pdgfra* and *Tcf21* (Figures S6C and S6D) versus myofibroblast genes such as *Col1a1*, *Postn*, and *Acta2* (Figures S6A, S6E, and S6F). Epicardial clusters were also identified (F-EPI, F-EPI/MES, MYO-EPI, Figures 5B and 5C) that expressed transcriptional markers associated with quiescent epicardium (F-EPI), mesothelial, and epicardial states (F-EPI/MES) and activated epicardial states (MYO-EPI). Based on the bulk RNA-seq analysis in Figure 4T, we expected a unique fibroblast substate with an epicardial progenitor identity or an expansion of epicardial cells in the MBNL1-null population, but instead epicardial and epicardial/mesothelial cell clusters were completely absent in the Fl-Tcf21^{iCre} cardiac fibroblast population (Figures 5D, 5E, S6G, and S6H). These epicardial populations were expanded in NTGs, which we believe represents the normal epicardial reactivation and expansion that occurs between days 1 and 5 following MI (Quijada et al., 2020). To better understand the changes in epicardial subclusters and altered EMT gene expression in MBNL1-null cardiac fibroblasts, differential gene expression was analyzed for fibroblast clusters that expanded solely in Fl-Tcf21^{iCre} mice versus NTGs in response to MI (Figure S6H). Genes that defined these clusters were subjected to GO analysis, which produced a gene list enriched for the biological processes of mesenchymal stem cell differentiation (Figure S6I). Quiescent fibroblast clusters that were highly expressing both *Sca1* (*Ly6a*) and *Pdgfra* (F-SH2 and F-SH1) were significantly expanded in Fl-Tcf21^{iCre} mice (Figures S6J and S6K). The tandem features of heightened proliferation capacity (Figures 4O and 4P) and expression of both *Sca1* and *Pdgfra* (Figures S6J and S6K) are hallmarks of cardiac mesenchymal stem cells (Chong et al., 2011; Noseda et al., 2015; White and Chong, 2020). GO analysis also showed that these clusters were enriched for factors that differentiate into other mesenchymal lineages, such as melanocytes, connective tissue, and coronary vasculature (Figure S6I), suggesting that the Fl-Tcf21^{iCre} quiescent fibroblast population becomes enriched for mesenchymal stem cell properties upon injury. Notably, these cells do not have the identity of conventional bone-marrow-derived mesenchymal stem cells but rather have markers and behaviors akin to those from the heart, which are pro-repair (Chong et al., 2011; Noseda et al., 2015; White and Chong, 2020).

Pseudotime analysis was performed using *a priori* knowledge of fibroblastic states to anchor pseudotime in F-SH2 and F-EPI based on expression of more immature/quiescent factors. Pseudotemporal ordering revealed that quiescent cells transit through F-ACT, MYO-EPI, and MYO-2 states on their lineage trajectory to the most mature myofibroblast state MYO-1 (Figures 5C, S6L, and

S6M). Relative to NTGs, over 40% of MBNL1 Tg cardiac fibroblasts are found in the larger activated myofibroblast cluster (MYO-1, MYO-2, and F-ACT), with the bulk of cells residing in the most mature MYO-1 state in the sham condition (Figures 5D, 5E, and S6G), which is described by the increased expression of the fibrotic ECM and maturation genes such as *Mgp*, *Sparc*, *Mfap5*, *Cst3*, *Bgn*, *Postn*, and *Cilp* (Figures 5C, S6N, and S6O). Many of these transcripts, such as *Mgp* (bound and upregulated), *Cst3* (bound, undefined regulation), *Bgn* (bound and spliced), and *Postn* (bound, undefined regulation) are directly bound and regulated by MBNL1 (Figures 5C, S1A, S6N, and S6O). Following MI, the MBNL1 transgene transitioned 60% of the cardiac fibroblasts to the mature MYO-1 state with a very small fraction residing in myofibroblast intermediates (Figures 5D, 5E, S6G, and S6H). This contrasts with NTG cardiac fibroblasts, which primarily shift to an intermediate activated state (F-ACT) following MI (Figures 5D, 5E, S6G, and S6H). Moreover, in the MI condition, NTGs still retain a quiescent population, which is nearly depleted in MBNL1 Tg-Tcf21^{iCre} mice (Figures 5D, 5E, S6G, and S6H). This suggests that MBNL1 in tandem with injury pushes quiescent fibroblasts into the most mature myofibroblastic state. The effects of MBNL1 loss of function (Fl-Tcf21^{iCre}) following MI are even more striking, as the entire cardiac fibroblast population remain stuck in quiescence (Figures 5D, 5E, S6G, and S6H). In addition, MI triggered a quiescent substate expansion in Fl-Tcf21^{iCre} hearts (Figures 5D, 5E, S6G, and S6H), which may be due to the enhanced proliferation and/or differentiation defects (Figure 4). Comparisons of Tg and null cardiac fibroblasts by both scRNA-seq and bulk RNA-seq data sets (Figures 5D, 5E, S4G, S5D, S6N, and S6O) show that gain and loss of MBNL1 function elicited diametrically opposed fate decisions.

MBNL1 maintains the myofibroblastic state

MBNL1's role in inducing cardiac fibroblast state transitions is becoming clear, but whether it is essential for maintaining myofibroblast activity is unknown. To address this, a *Postn*^{iCre} driver excised MBNL1 from activated myofibroblasts in MBNL1^{Fl/Fl}-*Postn*^{iCre} mice (Figure 6A) with a 10-day treatment of Tam beginning 2 days after injury (Figure 6B). Unlike Fl-Tcf21^{iCre} mice, MBNL1^{Fl/Fl}-*Postn*^{iCre} mice had a slight but insignificant reduction in α SMA⁺ myofibroblasts numbers (Figures 4I, 4J, 6C, and 6D), yet still had a significant decrease in the overall fibrotic response (Figures 6E and 6F). Curiously, MBNL1^{Fl/Fl}-*Postn*^{iCre} mice had no change in ECM maturity when compared with their MBNL1^{Fl/Fl} littermates (Figures 6G and 6H), although differences in scar maturity typically occur later in repair. MBNL1^{Fl/Fl}-*Postn*^{iCre} mice had preserved systolic function and were protected from adverse myocardial remodeling (Figures 6I–6K). These data demonstrated that myofibroblast-restricted excision of MBNL1 functionally protects against MI-induced fibrotic and maladaptive cardiac remodeling.

Stabilization of Sox9 rescues myofibroblast differentiation in MBNL1-null cardiac fibroblasts

To identify the MBNL1-regulated transcripts driving changes in the cardiac fibroblast state following MI, three data sets were mined for: factors bound by MBNL1, inducers of myofibroblast differentiation, and transcripts downregulated in Fl-Tcf21^{iCre} cardiac fibroblasts after MI (Figure S1; Davis et al., 2015). The only

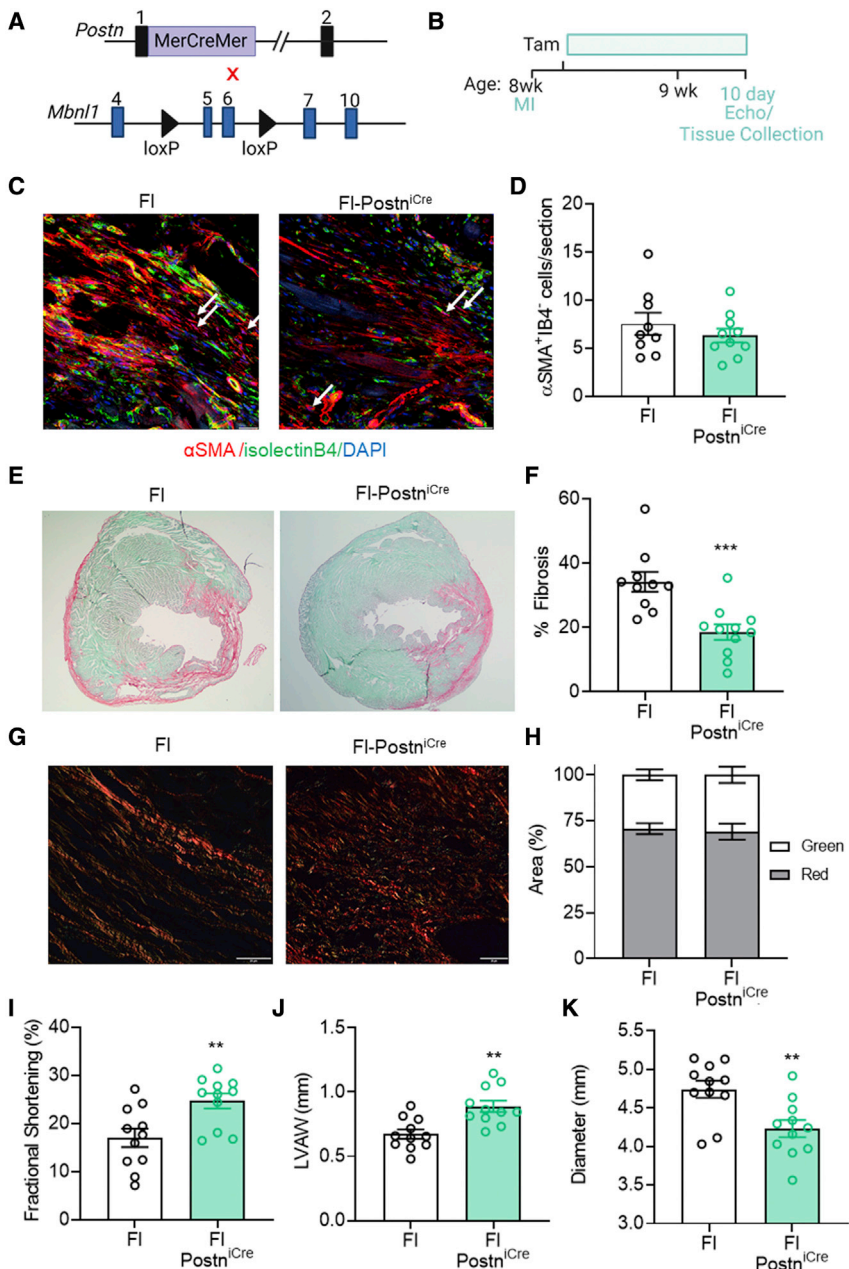


Figure 6. Myofibroblast-specific expression of MBNL1 is required for fibrotic scarring

(A) Breeding scheme for cardiac myofibroblast-specific MBNL1 knockout mice (MBNL1^{Fl/Fl}-Postn^{iCre}): (top) Postn^{iCre} knockin mice, (bottom) conditional *Mbnl1* knockout mice (MBNL1^{Fl/Fl}). (B) Timeline of Tam dosing, MI, and experimental endpoints.

(C and D) (C) Immunofluorescent imaging and (D) quantification of myofibroblasts in myocardial sections from mice 10 days following MI. Myofibroblasts are α SMA (red) positive and negative for the endothelial marker isolectinB4 (green). Nuclei are blue. Arrows show α SMA⁺IB4⁻ cells. Scale bars, 25 μ m. Dots are biological replicates, MBNL1^{Fl/Fl}-Postn^{iCre} (n = 10), MBNL1^{Fl/Fl} (n = 8), bars are mean \pm SEM, unpaired t tests, p = 0.3734.

(E and F) (E) Images and (F) quantification of fibrosis from Sirius red/fast green-stained myocardial sections. Dots are biological replicates, bars are mean \pm SEM, unpaired t tests, ***p < 0.001.

(G and H) (G) Images and (H) quantification of collagen birefringence in MBNL1^{Fl/Fl}-Tcf21^{iCre} (n = 4), MBNL1^{Fl/Fl} (n = 4) myocardial sections. Scale bars, 20 μ m. Bars are mean \pm SEM, unpaired t tests, p = 0.7574.

(I-K) Quantification of left ventricular (I) fractional shortening, (J) anterior wall thickness, and (K) diastolic diameter 10 days post MI. Dots are biological replicates, MBNL1^{Fl/Fl}-Postn^{iCre} (n = 10) and MBNL1^{Fl/Fl} (n = 8) mice, bars are mean \pm SEM, unpaired t tests, **p < 0.01.

gene meeting all three criteria was Sox9, a transcription factor essential for EMT and myofibroblast formation (Figure 7A; Lacraz et al., 2017; Scharf et al., 2019). Sox9 expression increased 8.5-fold and remained elevated in wild-type Postn⁺ myofibroblasts relative to quiescent fibroblasts following injury (Figure 7B). By contrast, the percentage of Sox9⁺, PDGFR α ⁺ fibroblasts was reduced 2.5-fold in infarcted Fl-Tcf21^{iCre} hearts (Figures 7C and 7D). Transfection of Sox9 into MBNL1^{Fl/Fl} and Fl-Tcf21^{iCre} cardiac fibroblasts was sufficient to induce α SMA⁺ myofibroblasts independent of genotype *in vitro*, demonstrating Sox9 alone promotes a myofibroblastic state and that it can rescue differentiation defects in MBNL1-null fibroblasts (Figures 7E and 7F). Previous studies have demonstrated that MBNL1 binds

and regulates Sox9 (Davis et al., 2015; Girardot et al., 2018), and these findings were confirmed in cardiac fibroblasts by RNA immunoprecipitation assay (Figure 7G). As Sox9 is upregulated in conjunction with MBNL1 expression (Figures 1J and 7B), it was hypothesized that MBNL1 stabilizes Sox9 transcripts. To test this hypothesis, mRNA decay assays were performed in MBNL1^{Fl/Fl} and Fl-Tcf21^{iCre} cardiac fibroblasts. Here, Sox9 and *Mbnl1* expression was measured as a function of exposure to the transcription inhibitor actinomycin D (Figures 7H and 7I). At time 0, the Fl-Tcf21^{iCre} fibroblasts had 53% less

Sox9 expression relative to the MBNL1^{Fl/Fl} controls as well as faster transcript decay (Figure 7H). Adenoviral transduction of MBNL1 (AdMBNL1) rescued Sox9 expression, which slowed the actinomycin D-mediated decay rate in both genotypes (Figure 7H). These data suggest that following MI, MBNL1 stabilizes the Sox9 transcripts in cardiac fibroblasts to promote myofibroblast state transitions.

DISCUSSION

Results from this study confirmed MBNL1's requirement in the heart's fibrotic response through its reprogramming of the cardiac fibroblast transcriptome during wound healing, while

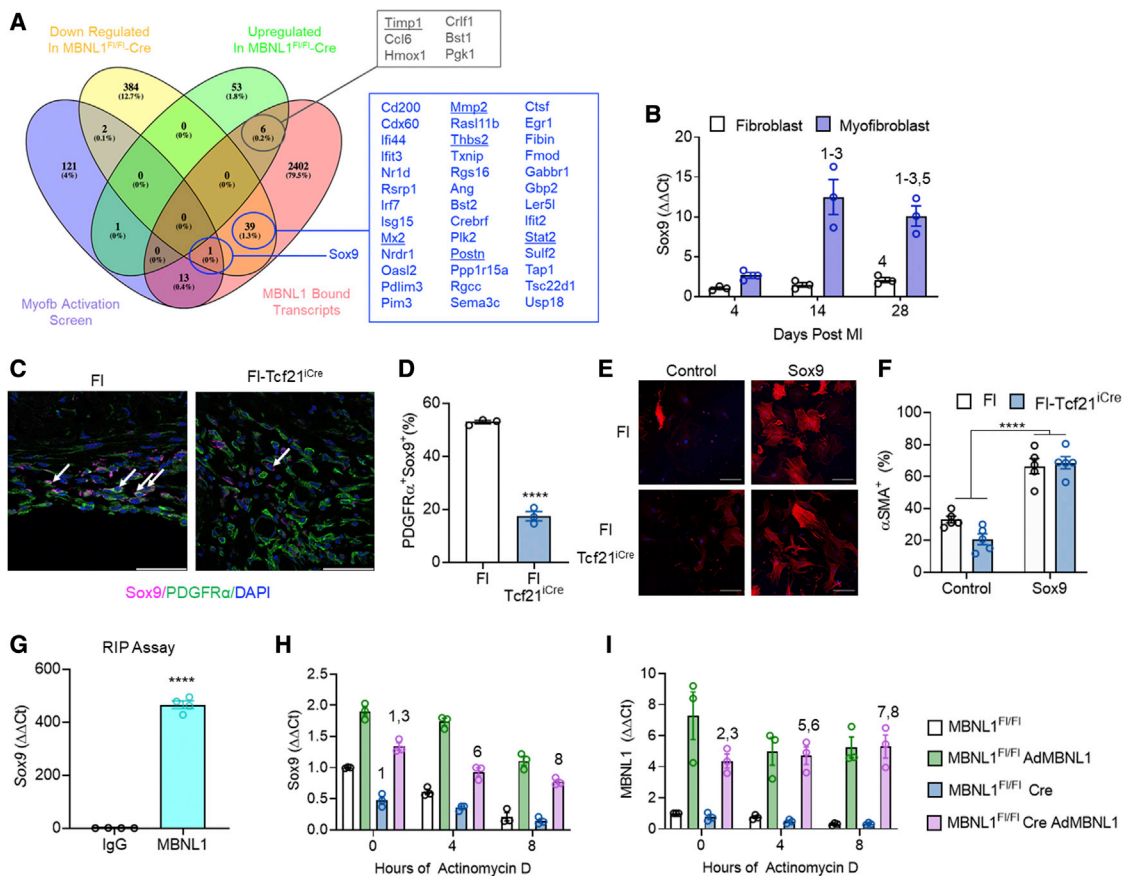


Figure 7. $MBNL1$ stabilization of $Sox9$ promotes myofibroblast formation

(A) Venn diagram showing the overlap between $MBNL1$ regulated transcripts (pink oval), positive inducers of myofibroblast differentiation (purple oval) (Davis et al., 2015), and genes downregulated in $MBNL1^{F/F}$ - $Tcf21^{iCre}$ cardiac fibroblasts (yellow oval).

(B) Fold change in $Sox9$ gene expression in cardiac myofibroblasts and quiescent fibroblasts relative to day-4 quiescent fibroblasts by the $\Delta\Delta Ct$ method. 18S was used for normalization. Dots are biological replicates, $n = 3$ mice per group, bars are mean \pm SEM, ANOVA statistical test with Tukey post hoc comparisons, numbers represent significant pairwise comparisons at $p < 0.05$: (1) 4-day fibroblast, (2) 4-day myofibroblast, (3) 14-day fibroblast, (4) 14-day myofibroblast, (5) 28-day fibroblast, and (6) 28-day myofibroblast.

(C and D) (C) Immunofluorescent imaging and (D) quantification of $Sox9^+$, $PDGFR\alpha^+$ fibroblasts in myocardial sections from $MBNL1^{F/F}$ - $Tcf21^{iCre}$ ($n = 3$), $MBNL1^{F/F}$ ($n = 3$) mice 14 days following MI. Data are the percentage of $PDGFR\alpha^+$ (green) fibroblasts co-stained with $Sox9$ (magenta). Nuclei are blue. White arrows show $PDGFR\alpha^+$, $Sox9^+$ cells. Scale bars, 50 μ m. Dots are biological replicates, bars are mean \pm SEM, unpaired t tests, *** $p < 0.0001$.

(E and F) (E) Immunofluorescent images and (F) quantification of α SMA $^+$ (red) in $MBNL1^{F/F}$ - $Tcf21^{iCre}$ and $MBNL1^{F/F}$ cardiac fibroblasts transfected with $Sox9$ / plasmid. Dots are biological replicates, $n = 5$ per group, bars are mean \pm SEM, ANOVA statistical test with Tukey post hoc comparisons, *** $p < 0.0001$.

(G) Expression of $Sox9$ transcripts immunoprecipitated by $MBNL1$ in fibroblasts overexpressing $MBNL1$. Dots represent biological replicates and bars represent mean \pm SEM, unpaired t test *** $p < 0.0001$.

(H and I) (H) $Sox9$ and (I) $Mbnl1$ gene expression in $MBNL1^{F/F}$ - $Tcf21^{iCre}$ and $MBNL1^{F/F}$ cardiac fibroblasts with or without Ad $MBNL1$ infection and actinomycin D treatment. Dots are biological replicates, $n = 3$ per condition, bars are mean \pm SEM, ANOVA with Tukey post hoc comparisons, numbers represent significant pairwise comparisons at $p < 0.05$: (1) 0 h FI, (2) 0 h FI Ad $MBNL1$, (3) 0 h FI-Cre, (4) 0 h FI-Cre Ad $MBNL1$, (5) 4 h Ad $MBNL1$, (6) 4 h FI-Cre, (7) 8 h FI Ad $MBNL1$, and (8) 8 h FI-Cre.

complementing our previous work with global $MBNL1$ knockouts that showed $MBNL1$ matures the myofibroblast transcriptome but failed to directly prove that fibrotic outcomes were due to its cardiac fibroblast-specific role (Davis et al., 2015). Here, cardiac fibroblast-targeted gain and loss of $MBNL1$ function provided the experimental proof that $MBNL1$ post-transcriptionally regulates an injury-induced fibroblast state dynamic, which in turn modulates maladaptive myocardial remodeling and the nature of fibrotic scarring. These positive outcomes were clearly linked to blocking myofibroblast state transitions and possibly due to low matrifibrocyte numbers as these cells

derive from the $Postn$ -lineage during scar maturation (Fu et al., 2018). Given that (1) there were greater reductions in fibrosis from deleting $MBNL1$ in $Postn^+$ myofibroblasts (Figures 6E and 6F), (2) $MBNL1$ expression increased at the time matrifibrocytes formed (Figure 1J), and (3) scars failed to mature, our hypothesis regarding defective matrifibrocyte function may indeed be true. However, these data cannot discriminate whether $MBNL1$ directly regulates matrifibrocyte state transitions or whether cardiac fibroblasts must first become myofibroblasts before transitioning into matrifibrocytes. Notably, unique matrifibrocyte clusters were not identified by scRNA-seq despite the increased

expression of matrifibrocyte transcripts within several fibroblast substates (Figures 5B–5E). However, this could be due to the timing of data collection, which was earlier than that described for matrifibrocyte formation (Fu et al., 2018).

Deleting MBNL1 expression in tandem with an injury signal not only prevented the development of all activated myofibroblast states but also expanded all possible quiescent substates, including those enriched for mesenchymal cell properties (Figures 4O–4U, 5A–5E, and S6G–S6K), characterized by heightened proliferation and expression of both *Sca1* and *Pdgfra* (Chong et al., 2011; Noseda et al., 2015; White and Chong, 2020). Other quiescent substates (F-SL1 and F-SL2) had enhanced expression of the cytokine *Il6* (Figure 5C) and transcription factor *Zbtb16*, which promotes the maintenance and renewal of stem cells (Liu et al., 2016). The expression of *Il6* by the F-SL1 fibroblasts suggests that this cluster has a proinflammatory function, while *Zbtb16* expression in the F-SL2 fibroblasts may renew and preserve the quiescent fibroblast population. Fl-Tcf21^{iCre} mice also had a larger F-WNTx cluster (Figure S6H), which was previously defined as antifibrotic and reparative (Farbehi et al., 2019). Moreover, an F-THSD7 substate was identified and expanded in Fl-Tcf21^{iCre} mice in response to MI (Figures 5C–5E, S6G, and S6H). This cluster was defined by upregulated epicardial transcripts and thus believed to partially underlie the redeployment of developmental and EMT signals detected in the MBNL1-null fibroblasts by bulk RNA-seq (Figures 4T and 4U). We postulate that the expansion of these quiescent clusters in Fl-Tcf21^{iCre} mice likely underlies their improved outcomes following MI, due to the pro-repair, angiogenic, and antifibrotic qualities of these various fibroblast clusters (Figure 5).

Despite the significant changes to the transcriptome at baseline, MBNL1 Tg-Tcf21^{iCre} mice lacked a corresponding induction of cardiac fibrosis with only 2 weeks of transgene activation. One explanation for this finding is that, without a stressor, ECM degradation and clearance mechanisms may keep up with production at this early time point. However, studies with other inducers of the myofibroblast fate, such as MKK6 and YAP, caused a fibrotic phenotype shortly after transgene induction (Bugg et al., 2020; Molkentin et al., 2017; Xiao et al., 2019), suggesting there are additional levels of regulation between transcriptional phenotype and physiologic function that are required for producing fibrotic ECM (Figure 2). It is also possible that forced expression of MBNL1 simply primes the fibroblast transcriptome by lowering the activation energy needed to destabilize quiescence, and then subsequent perturbations (i.e., injury or stiffness) are needed to achieve physiologic myofibroblast states (Figures 2L, 3, and 5E).

Surprisingly, forced MBNL1 expression in cardiac fibroblasts impacted the MI-induced left ventricular function and remodeling before significant changes to the ECM were observed (Figures 3E–3J). While this change in whole heart function was not due to enhanced myocyte death, Tg fibroblasts induced greater myocyte dilation (Figures 3K, 3N, and 3O), which likely underlies the poor systolic function in these animals. Each fibroblast cluster was surveyed for the expression of secreted factors or cytokines unique to the expanded myofibroblast populations in MBNL1 Tg-Tcf21^{iCre} mice as a driver of this remodeling, but no factor stood out as a candidate (Figure S7A). Interestingly, *Fstl1*, which was previously shown to prevent myocyte

apoptosis and maladaptive remodeling (Oshima et al., 2008; Shimano et al., 2011), was upregulated in the MYO-1 substate, the predominant cluster in MBNL1 Tg mice (Figures S6G and S6H), and RNA immunoprecipitation assays demonstrated MBNL1 binds *Fstl1* (Figure S7B). While *Fstl1* may have contributed to preventing excessive apoptosis in MBNL1 Tg-Tcf21^{iCre} mice, diastolic remodeling at the myocyte level was accentuated by still unknown mechanisms.

MBNL1 regulates many transcripts promoting cardiac fibroblast to myofibroblast state transitions (Davis et al., 2015), and here we found that MBNL1-dependent stabilization of *Sox9* mRNA was a contributing mechanism (Figure 7). Indeed, this transcription factor is essential for the fibrotic and inflammatory response to ischemic injury (Lacraz et al., 2017; Ruiz-Villalba et al., 2020; Scharf et al., 2019), likely through its role in regulating the expression of key EMT and ECM genes needed for cardiac repair (Lacraz et al., 2017; Akiyama et al., 2004; Lincoln et al., 2007). Collectively, these findings strongly implicate MBNL1's regulation of *Sox9* as an essential determinant of fibrotic state transitions and the nature of ECM remodeling.

The ability to control myofibroblast reversibility holds great promise for addressing the clinical burden of fibrosis, given that preventing the induction and maintenance of myofibroblast activity by pharmacologic or genetic means can significantly prevent fibrotic remodeling in the heart and other tissues (Bugg et al., 2020; Davis et al., 2012, 2015; Dobaczewski et al., 2010; Huang et al., 2019; Koitabashi et al., 2011; Lighthouse et al., 2019; Molkentin et al., 2017; Small et al., 2010). Targeting post-transcriptional mechanisms underlying fibroblast plasticity is an appealing approach as approximately one-third of the changes in gene expression are subject to post-transcriptional regulation affecting overall protein abundance (Chothani et al., 2019). MBNL1 has desirable therapeutic qualities, as it regulates multiple facets of fibroblast function required for cardiac wound healing and repair.

Limitations of the study

The aim of this study was to understand the fibroblast-specific role of MBNL1 in regulating the heart's fibrotic response. We identified that MBNL1 was necessary for inducing and maintaining fibroblast to myofibroblast state transitions. More extensive studies using lineage-traced fibroblasts from MBNL1^{Fl/Fl}-Postn^{iCre} mice would provide greater insight into the range of fibroblast plasticity and its dependence on MBNL1 transcriptome maturation. Additional studies are also needed to understand the fibroblast-specific role of MBNL1 in regulating cell state transitions in chronic stress models where the fibroblast cell state might be more plastic. With respect to the *Sox9* mechanism, *in vivo* evidence that *Sox9* can rescue the heart's fibrotic response in MBNL1^{Fl/Fl} Tcf21^{iCre} mice is still warranted. Together, this information would allow better understanding of the therapeutic potential of RNA-binding proteins in managing cardiac fibrosis.

STAR★METHODS

Detailed methods are provided in the online version of this paper and include the following:

- KEY RESOURCES TABLE

● RESOURCE AVAILABILITY

- Lead contact
- Materials availability
- Data and code availability

● EXPERIMENTAL MODEL AND SUBJECT DETAILS

● METHOD DETAILS

- Animal models
- Surgical Model of Myocardial Infarction
- *In vivo* proliferation following MI
- Human primary cardiac fibroblast isolation
- Mouse primary cardiac fibroblast isolation
- In vitro cell treatments
- Collagen gel contraction assay
- Transcript stability assay
- Flow cytometry for fibroblast purification
- Single cell RNA sequencing and analysis
- Cardiomyocyte isolation
- Myocyte morphology tracing
- Measurements of myocyte contractility
- Gene expression analysis
- Bulk RNA Sequencing (RNAseq)
- Western blot
- Histology and immunohistochemistry
- Immunocytochemistry
- Image analysis
- Analysis of collagen birefringence
- RNA immunoprecipitation in cardiac fibroblasts
- Decellularization and collagen alignment analysis

● QUANTIFICATION AND STATISTICAL ANALYSIS

SUPPLEMENTAL INFORMATION

Supplemental information can be found online at <https://doi.org/10.1016/j.stem.2022.01.012>.

ACKNOWLEDGMENTS

This work was supported by grants from the National Institutes of Health for J.D. (HL141187 and HL142624) and C.A.D. (R35GM138036), Biological Mechanisms of Healthy Aging T32 for D.B. (T32AG066574), and Graduate Research Fellowships from the National Science Foundation for R.C.B. and I.M.R. (DGE-1762114).

AUTHOR CONTRIBUTIONS

D.B., L.R.J.B., R.C.B., K.E.B., I.M.R., K.Z.R., A.R., J.G., G.F., A.S.-O., C.A.D., and J.D. conducted experiments and analyzed results. Experiments were designed by D.B. and J.D. D.B., C.A.D., and J.D. contributed to writing and reviewing the manuscript.

DECLARATION OF INTERESTS

The authors declare no competing interests.

Received: February 2, 2021

Revised: November 30, 2021

Accepted: January 24, 2022

Published: February 16, 2022

REFERENCES

- Acharya, A., Baek, S.T., Banfi, S., Eskiocak, B., and Tallquist, M.D. (2011). Efficient inducible Cre-Mediated recombination in Tcf 21 cell lineages in the heart and kidney. *Genesis* **49**, 870–877.
- Acharya, A., Baek, S.T., Huang, G., Eskiocak, B., Goetsch, S., Sung, C.Y., Banfi, S., Sauer, M.F., Olsen, G.S., Duffield, J.S., et al. (2012). The bHLH transcription factor Tcf21 is required for lineage-specific EMT of cardiac fibroblast progenitors. *Development* **139**, 2139–2149.
- Afgan, E., Baker, D., Batut, B., Van Den Beek, M., Bouvier, D., Cech, M., Chilton, J., Clements, D., Coraor, N., Grüning, B.A., et al. (2018). The Galaxy platform for accessible, reproducible and collaborative biomedical analyses: 2018 update. *Nucleic Acids Res* **46**, W537–W544.
- Ahlmann-Eltze, C., and Huber, W. (2021). glmGamPoi: fitting Gamma-Poisson generalized linear models on single cell count data. *Bioinformatics* **36**, 5701–5702.
- Akiyama, H., Chaboissier, M.C., Behringer, R.R., Rowitch, D.H., Schedl, A., Epstein, J.A., and De Crombrugge, B. (2004). Essential role of Sox9 in the pathway that controls formation of cardiac valves and septa. *Proc. Natl. Acad. Sci. USA* **101**, 6502–6507.
- Alexanian, M., Przytycki, P.F., Micheletti, R., Padmanabhan, A., Ye, L., Travers, J.G., Gonzalez-Teran, B., Silva, A.C., Duan, Q., Ranade, S.S., et al. (2021). A transcriptional switch governs fibroblast activation in heart disease. *Nature* **595**, 438–443.
- Holmes, J.W., Nuñez, J.A., and Covell, J.W. (1997). Functional implications of myocardial scar structure. *Am. J. Physiol.* **272**, H2123–H2130.
- Batra, R., Charizanis, K., Manchanda, M., Mohan, A., Li, M., Finn, D.J., Goodwin, M., Zhang, C., Sobczak, K., Thornton, C.A., et al. (2014). Loss of MBNL leads to disruption of developmentally regulated alternative polyadenylation in RNA-mediated disease. *Mol. Cell* **56**, 311–322.
- Bretherton, R., Bugg, D., Olszewski, E., and Davis, J. (2020). Regulators of cardiac fibroblast cell state. *Matrix Biol* **91–92**, 117–135.
- Bugg, D., Bretherton, R., Kim, P., Olszewski, E., Nagle, A., Schumacher, A.E., Chu, N., Gunaje, J., Deforest, C.A., Stevens, K., et al. (2020). Infarct collagen topography regulates fibroblast fate via p38-yes-associated protein transcriptional enhanced associate domain signals. *Circ. Res.* **127**, 1306–1322.
- Butler, A., Hoffman, P., Smibert, P., Papalex, E., and Satija, R. (2018). Integrating single-cell transcriptomic data across different conditions, technologies, and species. *Nat. Biotechnol.* **36**, 411–420.
- Cao, J., and Poss, K.D. (2018). The epicardium as a hub for heart regeneration. *Nat. Rev. Cardiol.* **15**, 631–647.
- Carlson, S., Helterline, D., Asbe, L., Dupras, S., Minami, E., Farris, S., and Stempien-Otero, A. (2017). Cardiac macrophages adopt profibrotic/M2 phenotype in infarcted hearts: role of urokinase plasminogen activator. *J. Mol. Cell. Cardiol.* **108**, 42–49.
- Cheng, A.W., Shi, J., Wong, P., Luo, K.L., Trepman, P., Wang, E.T., Choi, H., Burge, C.B., and Lodish, H.F. (2014). Muscleblind-like 1 (Mbnl1) regulates pre-mRNA alternative splicing during terminal erythropoiesis. *Blood* **124**, 598–610.
- Chong, J.J.H., Chandranthan, V., Xaymardan, M., Asli, N.S., Li, J., Ahmed, I., Heffernan, C., Menon, M.K., Scarlett, C.J., Rashidianfar, A., et al. (2011). Adult cardiac-resident MSC-like stem cells with a proepicardial origin. *Cell Stem Cell* **9**, 527–540.
- Chothoni, S., Schäfer, S., Adam, E., Viswanathan, S., Widjaja, A.A., Langley, S.R., Tan, J., Wang, M., Quaife, N.M., Jian Pua, C., et al. (2019). Widespread translational control of fibrosis in the human heart by RNA-binding proteins. *Circulation* **140**, 937–951.
- Daseke, M.J., Tenkorang, M.A.A., Chalise, U., Konfrst, S.R., and Lindsey, M.L. (2020). Cardiac fibroblast activation during myocardial infarction wound healing: fibroblast polarization after MI. *Matrix Biol* **91–92**, 109–116.
- Davis, J., Burr, A.R., Davis, G.F., Birnbaumer, L., and Molkentin, J.D. (2012). A TRPC6-dependent pathway for myofibroblast transdifferentiation and wound healing *in vivo*. *Dev. Cell* **23**, 705–715.
- Davis, J., and Molkentin, J.D. (2014). Myofibroblasts: trust your heart and let fate decide. *J. Mol. Cell. Cardiol.* **70**, 9–18.
- Davis, J., Salomonis, N., Ghearing, N., Lin, S.-C.J., Kwong, J.Q., Mohan, A., Swanson, M.S., and Molkentin, J.D. (2015). MBNL1-mediated regulation of differentiation RNAs promotes myofibroblast transformation and the fibrotic response. *Nat. Commun.* **6**, 10084.

- Dobaczewski, M., Bujak, M., Li, N., Gonzalez-Quesada, C., Mendoza, L.H., Wang, X.F., and Frangogiannis, N.G. (2010). Smad3 signaling critically regulates fibroblast phenotype and function in healing myocardial infarction. *Circ. Res.* **107**, 418–428.
- Farbehi, N., Patrick, R., Dorison, A., Xaymardan, M., Janbandhu, V., Wystub-Lis, K., Ho, J.W.K., Nordon, R.E., and Harvey, R.P. (2019). Single-cell expression profiling reveals dynamic flux of cardiac stromal, vascular and immune cells in health and injury. *Elife* **8**, e43882.
- Farris, S.D., Don, C., Helterline, D., Costa, C., Plummer, T., Steffes, S., Mahr, C., Mokadam, N.A., and Stempien-Otero, A. (2017). Cell-specific pathways supporting persistent fibrosis in heart failure. *J. Am. Coll. Cardiol.* **70**, 344–354.
- Fu, X., Khalil, H., Kanisicak, O., Boyer, J.G., Vagnozzi, R.J., Maliken, B.D., Sargent, M.A., Prasad, V., Valiente-Alandi, I., Blaxall, B.C., et al. (2018). Specialized fibroblast differentiated states underlie scar formation in the infarcted mouse heart. *J. Clin. Invest.* **128**, 2127–2143.
- Girardot, M., Bayet, E., Maurin, J., Fort, P., Roux, P., and Raynaud, P. (2018). SOX9 has distinct regulatory roles in alternative splicing and transcription. *Nucleic Acids Res* **46**, 9106–9118.
- von Gise, A., and Pu, W.T. (2012). Endocardial and epicardial epithelial to mesenchymal transitions in heart development and disease. *Circ. Res.* **110**, 1628–1645.
- Hafemeister, C., and Satija, R. (2019). Normalization and variance stabilization of single-cell RNA-seq data using regularized negative binomial regression. *Genome Biol* **20**, 296.
- Hegyi, B., Borst, J.M., Bailey, L.R.J., Shen, E.Y., Lucena, A.J., Navedo, M.F., Bossuyt, J., and Bers, D.M. (2020). Hyperglycemia regulates cardiac K⁺ channels via O-GlcNAc-CaMKII and NOX2-ROS-PKC pathways. *Basic Res Cardiol.* **115**, 71.
- Huang, G.N., Thatcher, J.E., McAnally, J., Kong, Y., Qi, X., Tan, W., DiMaio, J.M., Amatruda, J.F., Gerard, R.D., Hill, J.A., et al. (2012). C/EBP transcription factors mediate epicardial activation during heart development and injury. *Science* **338**, 1599–1603.
- Huang, S., Chen, B., Su, Y., Alex, L., Humeres, C., Shinde, A.V., Conway, S.J., and Frangogiannis, N.G. (2019). Distinct roles of myofibroblast-specific Smad2 and Smad3 signaling in repair and remodeling of the infarcted heart. *J. Mol. Cell. Cardiol.* **132**, 84–97.
- Kanisicak, O., Khalil, H., Ivey, M.J., Karch, J., Maliken, B.D., Correll, R.N., Brody, M.J., Lin, S.-C.J., Aronow, B.J., Tallquist, M.D., et al. (2016). Genetic lineage tracing defines myofibroblast origin and function in the injured heart. *Nat. Commun.* **7**, 12260.
- Kim, D., Paggi, J.M., Park, C., Bennett, C., and Salzberg, S.L. (2019). Graph-based genome alignment and genotyping with HISAT2 and HISAT-genotype. *Nat. Biotechnol.* **37**, 907–915.
- Koitabashi, N., Danner, T., Zaiman, A.L., Pinto, Y.M., Rowell, J., Mankowski, J., Zhang, D., Nakamura, T., Takimoto, E., and Kass, D.A. (2011). Pivotal role of cardiomyocyte TGF-β signaling in the murine pathological response to sustained pressure overload. *J. Clin. Invest.* **121**, 2301–2312.
- Kolberg, L., Raudvere, U., Kuzmin, I., Vilo, J., and Peterson, H. (2020). gprofiler2—an R package for gene list functional enrichment analysis and name-space conversion toolset g:profiler. *F1000Res.* **9**, 709.
- Lacraz, G.P.A.A., Junker, J.P., Gladka, M.M., Molenaar, B., Scholman, K.T., Vigil-Garcia, M., Versteeg, D., de Ruiter, H., Vermunt, M.W., Creyghton, M.P., et al. (2017). Tomo-Seq identifies SOX9 as a key regulator of cardiac fibrosis during ischemic injury. *Circulation* **136**, 1396–1409.
- Liao, Y., Smyth, G.K., and Shi, W. (2014). FeatureCounts: an efficient general purpose program for assigning sequence reads to genomic features. *Bioinformatics* **30**, 923–930.
- Lighthouse, J.K., Burke, R.M., Velasquez, L.S., Dirkx, R.A., Aiezza, A., Moravec, C.S., Alexis, J.D., Rosenberg, A., and Small, E.M. (2019). Exercise promotes a cardioprotective gene program in resident cardiac fibroblasts. *JCI Insight* **4**, e92098.
- Lincoln, J., Kist, R., Scherer, G., and Yutzy, K.E. (2007). Sox9 is required for precursor cell expansion and extracellular matrix organization during mouse heart valve development. *Dev. Biol.* **305**, 120–132.
- Liu, T.M., Lee, E.H., Lim, B., and Shyh-Chang, N. (2016). Concise review: balancing stem cell self-renewal and differentiation with PLZF. *Stem Cells* **34**, 277–287.
- Liu, Y., Cseresnyés, Z., Randall, W.R., and Schneider, M.F. (2001). Activity-dependent nuclear translocation and intranuclear distribution of NFATc in adult skeletal muscle fibers. *J. Cell Biol.* **155**, 27–39.
- Liu, Y., Keikhosravi, A., Mehta, G.S., Drifka, C.R., and Eliceiri, K.W. (2017). Methods for quantifying fibrillar collagen alignment. *Methods Mol. Biol.* **1627**, 429–451.
- Love, M.I., Huber, W., and Anders, S. (2014). Moderated estimation of fold change and dispersion for RNA-seq data with DESeq2. *Genome Biol* **15**, 550.
- McInnes, L., Healy, J., and Melville, J. (2018). t-SNE: uniform manifold approximation and projection for dimension reduction. Preprint in arXiv, 03426, arXiv:1802.03311.
- Molkentin, J.D., Bugg, D., Ghearing, N., Dorn, L.E., Kim, P., Sargent, M.A., Gunaje, J., Otsu, K., and Davis, J. (2017). Fibroblast-specific genetic manipulation of p38 MAPK *in vivo* reveals its central regulatory role in fibrosis. *Circulation* **136**, 549–561.
- Mouton, A.J., Ma, Y., Rivera Gonzalez, O.J., Daseke, M.J., Flynn, E.R., Freeman, T.C., Garrett, M.R., DeLeon-Pennell, K.Y., and Lindsey, M.L. (2019). Fibroblast polarization over the myocardial infarction time continuum shifts roles from inflammation to angiogenesis. *Basic Res. Cardiol.* **114**, 6.
- Muzumdar, M.D., Tasic, B., Miyamichi, K., Li, L., and Luo, L. (2007). A global double-fluorescent Cre reporter mouse. *Genesis* **45**, 593–605.
- Ngo, P., Ramalingam, P., Phillips, J.A., and Furuta, G.T. (2006). Collagen gel contraction assay. *Methods Mol. Biol.* **341**, 103–109.
- Noseda, M., Harada, M., McSweeney, S., Leja, T., Belian, E., Stuckey, D.J., Abreu Paiva, M.S., Habib, J., Macaulay, I., de Smith, A.J., et al. (2015). PDGFR α demarcates the cardiogenic clonogenic Sca1+ stem/progenitor cell in adult murine myocardium. *Nat. Commun.* **6**, 6930.
- Oshima, Y., Ouchi, N., Sato, K., Izumiya, Y., Pimentel, D.R., and Walsh, K. (2008). Follistatin-like 1 is an Akt-regulated cardioprotective factor that is secreted by the heart. *Circulation* **117**, 3099–3108.
- Pascual, M., Vicente, M., Monferrer, L., and Artero, R. (2006). The muscleblind family of proteins: an emerging class of regulators of developmentally programmed alternative splicing. *Differentiation* **74**, 65–80.
- Pedregosa, F., Michel, V., Grisel, O., Blondel, M., Prettenhofer, P., Weiss, R., Vanderplas, J., Cournapeau, D., Pedregosa, F., Varoquaux, G., et al. (2011). Scikit-learn: machine learning in Python. *J. Mach. Learn. Res.* **12**, 2825–2830.
- Qiu, X., Mao, Q., Tang, Y., Wang, L., Chawla, R., Pliner, H.A., and Trapnell, C. (2017). Reversed graph embedding resolves complex single-cell trajectories. *Nat. Methods* **14**, 979–982.
- Quijada, P., Trembley, M.A., and Small, E.M. (2020). The role of the epicardium during heart development and repair. *Circ. Res.* **126**, 377–394.
- Quinn, K.P., Sullivan, K.E., Liu, Z., Ballard, Z., Siokatas, C., Georgakoudi, I., and Black, L.D. (2016). Optical metrics of the extracellular matrix predict compositional and mechanical changes after myocardial infarction. *Sci. Rep.* **6**, 35823.
- Raudvere, U., Kolberg, L., Kuzmin, I., Arak, T., Adler, P., Peterson, H., and Vilo, J. (2019). G:profiler: a web server for functional enrichment analysis and conversions of gene lists (2019 update). *Nucleic Acids Res* **47**, W191–W198.
- Richardson, W.J., Clarke, S.A., Quinn, T.A., and Holmes, J.W. (2015). Physiological implications of myocardial scar structure. *Compr. Physiol.* **5**, 1877–1909.
- Rueden, C.T., Schindelin, J., Hiner, M.C., DeZonia, B.E., Walter, A.E., Arena, E.T., and Eliceiri, K.W. (2017). ImageJ2: ImageJ for the next generation of scientific image data. *BMC Bioinformatics* **18**, 529.
- Ruiz-Villalba, A., Romero, J.P., Hernández, S.C., Vilas-Zornoza, A., Fortelny, N., Castro-Labrador, L., Martín-Uriz, P.S., Lorenzo-Vivas, E., García-Olloqui, P., Palacio, M., et al. (2020). Single-cell RNA sequencing analysis reveals a crucial role for CTHRC1 (collagen triple helix repeat containing 1) cardiac fibroblasts after myocardial infarction. *Circulation* **142**, 1831–1847.
- Savarese, G., and Lund, L.H. (2017). Global public health burden of heart failure. *Card. Fail. Rev.* **3**, 7–11.

- Scharf, G.M., Kilian, K., Cordero, J., Wang, Y., Grund, A., Hofmann, M., Froese, N., Wang, X., Kispert, A., Kist, R., et al. (2019). Inactivation of Sox9 in fibroblasts reduces cardiac fibrosis and inflammation. *JCI Insight* 5, e126721.
- Schindelin, J., Arganda-Carreras, I., Frise, E., Kaynig, V., Longair, M., Pietzsch, T., Preibisch, S., Rueden, C., Saalfeld, S., Schmid, B., et al. (2012). Fiji: an open-source platform for biological-image analysis. *Nat. Methods* 9, 676–682.
- Shimano, M., Ouchi, N., Nakamura, K., van Wijk, B., Ohashi, K., Asaumi, Y., Higuchi, A., Pimentel, D.R., Sam, F., Murohara, T., et al. (2011). Cardiac myocyte follistatin-like 1 functions to attenuate hypertrophy following pressure overload. *Proc. Natl. Acad. Sci. USA* 108, E899–E906.
- Sirén, J., Välimäki, N., and Mäkinen, V. (2014). Indexing Graphs for Path Queries with Applications in Genome Research. *IEEE/ACM Transactions on Computational Biology and Bioinformatics* 2014, 375–388.
- Skelly, D.A., Squiers, G.T., McLellan, M.A., Bolisetti, M.T., Robson, P., Rosenthal, N.A., and Pinto, A.R. (2018). Single-cell transcriptional profiling reveals cellular diversity and intercommunication in the mouse heart. *Cell Rep* 22, 600–610.
- Small, E.M., Thatcher, J.E., Sutherland, L.B., Kinoshita, H., Gerard, R.D., Richardson, J.A., Dimaio, J.M., Sadek, H., Kuwahara, K., and Olson, E.N. (2010). Myocardin-related transcription factor-a controls myofibroblast activation and fibrosis in response to myocardial infarction. *Circ. Res.* 107, 294–304.
- Stempien-Otero, A., Kim, D.H., and Davis, J. (2016). Molecular networks underlying myofibroblast fate and fibrosis. *J. Mol. Cell. Cardiol.* 97, 153–161.
- Stuart, T., and Srivastava, A. (2021). Building trajectories with Monocle 3 • Signac, <https://satijalab.org/signac/articles/monocle.html>.
- Trapnell, C., Cacchiarelli, D., Grimsby, J., Pokharel, P., Li, S., Morse, M., Lennon, N.J., Livak, K.J., Mikkelsen, T.S., and Rinn, J.L. (2014). The dynamics and regulators of cell fate decisions are revealed by pseudotemporal ordering of single cells. *Nat. Biotechnol.* 32, 381–386.
- Virtanen, P., Gommers, R., Oliphant, T.E., Haberland, M., Reddy, T., Cournapeau, D., Burovski, E., Peterson, P., Weckesser, W., Bright, J., et al. (2020). SciPy 1.0: fundamental algorithms for scientific computing in Python. *Nat. Methods* 17, 261–272.
- von Gise, A., Zhou, B., Honor, L.B., Ma, Q., Petryk, A., and Pu, W.T. (2011). WT1 regulates epicardial epithelial to mesenchymal transition through β -catenin and retinoic acid signaling pathways. *Dev. Biol.* 356, 421–431.
- Wang, E.T., Cody, N.A.L., Jog, S., Biancolella, M., Wang, T.T., Treacy, D.J., Luo, S., Schroth, G.P., Housman, D.E., Reddy, S., et al. (2012). Transcriptome-wide regulation of pre-mRNA splicing and mRNA localization by muscleblind proteins. *Cell* 150, 710–724.
- Waskom, M., Botvinnik, O., Ostblom, J., Gelbart, M., Lukauskas, S., Hobson, P., Gemperline, D.C., Augspurger, T., Halchenko, Y., Cole, J.B., et al. (2020). Mwaskom/seaborn: v0.10.1. <https://zenodo.org/record/3767070#.X3b-leORXIU>.
- White, S.J., and Chong, J.J.H. (2020). Mesenchymal stem cells in cardiac repair: effects on myocytes, vasculature, and fibroblasts. *Clin. Ther.* 42, 1880–1891.
- Wilkins, B.J., Dai, Y.S., Bueno, O.F., Parsons, S.A., Xu, J., Plank, D.M., Jones, F., Kimball, T.R., and Molkentin, J.D. (2004). Calcineurin/NFAT coupling participates in pathological, but not physiological, cardiac hypertrophy. *Circ. Res.* 94, 110–118.
- Willems, I.E., Havenith, M.G., Mey, J.G. de, and Daemen, M.J. (1994). The alpha-smooth muscle actin-positive cells in healing human myocardial scars. *Am. J. Pathol.* 145, 868–875.
- Xavier-Neto, J., Shapiro, M.D., Houghton, L., and Rosenthal, N. (2000). Sequential programs of retinoic acid synthesis in the myocardial and epicardial layers of the developing avian heart. *Dev. Biol.* 219, 129–141.
- Xiao, Y., Hill, M.C., Li, L., Deshmukh, V., Martin, T.J., Wang, J., and Martin, J.F. (2019). Hippo pathway deletion in adult resting cardiac fibroblasts initiates a cell state transition with spontaneous and self-sustaining fibrosis. *Genes Dev* 33, 1491–1505.
- Zheng, G.X.Y., Terry, J.M., Belgrader, P., Ryvkin, P., Bent, Z.W., Wilson, R., Ziraldo, S.B., Wheeler, T.D., McDermott, G.P., Zhu, J., et al. (2017). Massively parallel digital transcriptional profiling of single cells. *Nat. Commun.* 8, 14049.

STAR★METHODS

KEY RESOURCES TABLE

REAGENT or RESOURCE	SOURCE	IDENTIFIER
Antibodies		
Anti-Sox9	Millipore	Cat# AB5535, RRID:AB_2239761
Anti- α SMA	Sigma-Aldrich	Cat# A2547, RRID:AB_476701
Anti- α actinin	Sigma-Aldrich	Sigma-Aldrich Cat# A7811, RRID:AB_476766
Anti-GAPDH	Fitzgerald Industries International	Cat# 10R-2932, RRID:AB_11199818
Anti-Muscleblind-like 1 [MBNL1]	Abcam	Abcam Cat# ab45899, RRID:AB_1310475
Anti-PDGFR α	R and D Systems	Cat# AF1062, RRID:AB_2236897
Anti-WT1	Santa Cruz Biotechnology	Cat# sc-192, RRID:AB_632611
Anti-TBX18	Santa Cruz Biotechnology	Cat# sc-130428, RRID:AB_2303068
Anti-SLUG	Santa Cruz Biotechnology	Cat# sc-15391, RRID:AB_2191899
Isolectin B4	Vector Laboratories	Cat# FL-1201, RRID:AB_2314663
Wheat Germ Agglutinin	Thermo Fisher Scientific	Cat# :W11261
Anti-COL5A1	Santa Cruz Biotechnology	Cat# sc-166155, RRID:AB_2082963
Anti-COL3A1	Santa Cruz Biotechnology	Cat# sc-271249, RRID:AB_10613985
Cd11b-VioBlue, human and mouse	Miltenyi Biotec	Cat# 130-113-238, RRID:AB_2726047
Anti-Feeder Cells-APC, mouse	Miltenyi Biotec	Cat# 130-120-802, RRID:AB_2784336
Feeder Removal MicroBeads, mouse	Miltenyi Biotec	Cat#: 130-095-531
CD11b MicroBeads, human and mouse	Miltenyi Biotec	Cat#: 130-049-601
CD14 MicroBeads, human	Miltenyi Biotec	Cat#: 130-050-201
AlexaFluor Chicken Anti-Goat 488	Thermo Fisher Scientific	Cat# A-21467, RRID:AB_2535870
AlexaFluor Donkey Anti-Mouse 647	Thermo Fisher Scientific	Cat# A-31571, RRID:AB_162542
AlexaFluor Donkey Anti-Rabbit 647	Thermo Fisher Scientific	Cat# A-31573, RRID:AB_2536183
AlexaFluor Goat Anti-Mouse 568	Thermo Fisher Scientific	Cat# A-11004, RRID:AB_2534072
Rabbit-anti-FLAG	Sigma	Cat#: F7425
Rabbit IgG Isotype control	Cell Signaling Technologies	Cat#: 3900S
Hoechst	Invitrogen	Cat#: H3570
Goat anti-Mouse IgG Antibody, (H+L) HRP conjugate	Millipore Sigma	Cat #: AP308P
Goat anti-Rabbit IgG Antibody, (H+L) HRP conjugate	Millipore Sigma	Cat #:AP307P
Bacterial and virus strains		
AdMBNL1	(Davis et al., 2015)	N/A
AdSRF	(Davis et al., 2012)	N/A
Ad Δ Cna	(Wilkins et al., 2004)	N/A
AdGFP	(Liu et al., 2001)	N/A
Sox9 cDNA	Origene	Cat #: MC217147
pSV- β -galactosidase	Promega	Cat #: E1081
Chemicals, peptides, and recombinant proteins		
1M MgCl ₂	ThermoFisher	Cat #: AM9530G
1M Tris-HCl pH 7.4	ThermoFisher	Cat #: 15567027
2-Methylbutane (Certified ACS), Fisher Chemical	Fisher Scientific	Cat #: O3551-4
2,3-Butanedione monoxime (BDM)	Sigma	Cat #: B0753

(Continued on next page)

Continued

REAGENT or RESOURCE	SOURCE	IDENTIFIER
200 Micron Nylon Mesh Filter Woven Mesh Sheet Off-White Polyester Food Grade (50"x30")	Amazon	https://www.amazon.com/Micron-Nylon-Filter-Off-White-Polyester/dp/B07HYHHX5V/ref=sr_1_2?dchild=1&keywords=200+micron+mesh&qid=1611532184&sr=8-2
30% Acrylamid/Bis	Bio-Rad	Cat #: 1610156
5M NaCl	ThermoFisher	Cat #: AM9760G
Actinomycin D	Millipore Sigma	Cat #: A1410-2MG
Agarose	Fisher Scientific	Cat #: BP160-500
Biogenex Antigen Retrieval Citra Concentrated 10X	Biogenex	Cat #: HK086-9K
Blebbistatin	TRC Canada	Cat #: B592500
BSA	Fisher Scientific	Cat #: BP9705-100
Calcium Chloride Dihydrate	Fisher Scientific	Cat #: 10035-04-08
Characterized FBS	Fisher Scientific	Cat #: SH3007103
Cold Water Fish Skin Gelatin	Electron Microscopy Sciences	Cat #: 25560
Collagen from rat tail	Sigma Aldrich	Cat #: C7661
Collagenase Type 2	Worthington	Cat #: LS004176
Complete EDTA-free Protease Inhibitor Cocktail	Sigma	Cat #: 11836170001
D-(+)-Glucose	Sigma	Cat #: G7528-250G
D-Sucrose (Molecular Biology), Fisher BioReagents	Fisher Scientific	Cat #: 57-50-1
Digitonin	Promega	Cat #: G9441
Direct Red 80	Sigma Aldrich	Cat #: 365548
Dithiothreitol (DTT)	ThermoFisher	Cat #: 15508-013
DMEM High Glucose	Fisher Scientific	Cat #: 10-017-CV
DMSO	Fisher Scientific	Cat #: BP231-100
DNase I	Sigma Aldrich	Cat #: 260913-10MU
Dynabeads Protein A	ThermoFisher	Cat #: 10001D
EDTA	Fisher Scientific	Cat #: BP248250
EdU (5-ethynyl-2-deoxyuridine)	Life Technologies	Cat #: A10044
Ethanol	Fisher Scientific	Cat #: 04-355-223
Fast Green	Sigma Aldrich	Cat #: F7258
Formaldehyde 37%	Fisher Scientific (Ricca Chemical)	Cat #: RSO0010-4a
HBSS 1x with Calcium and Magnesium	Thermo Fisher	Cat #: 14025-092
HBSS 1x without Calcium and Magnesium	Fisher Scientific	Cat #: 21-022-CV
Heparin	Fresenius Kabi	N/A
Hepes	Fisher Scientific	Cat #: 7365-45-9
Horse Serum	Thermo Fisher	Cat #: 16050130
Isoflurane	Piramal	N/A
iTaq Universal Green SYBR	BioRad	Cat #: 1725124
KCl	Fisher Scientific	Cat #: P330
Ketamine	Zoetis	N/A
Laminin (Natural Mouse)	Gibco	Cat #: 23017-015
Liberase TH	Sigma Aldrich	Cat #: 5401151001
LS Columns	Miltenyi	Cat #: 130-042-401
Magnesium Sulfate Heptahydrate	Fisher Scientific	Cat #: 10034-99-8
Mowiol 4-88	Sigma Aldrich	Cat #: 81381-250G
Normal goat serum	Jackson Immunoresearch	Cat #: 005-000-121
NP-40	ThermoFisher	Cat #: 28324

(Continued on next page)

Continued

REAGENT or RESOURCE	SOURCE	IDENTIFIER
Opti-MEM I Reduced Serum Medium	Thermofisher	Cat #: 31985-062
Paraformaldehyde Solution, 4% in PBS, Thermo Scientific	Fisher Scientific	Cat #: AAJ19943K2
PBS power (10x)	Lifetechnologies	Cat #: 21300058
Peanut Oil	Planters	N/A
Penicillin-Streptomycin	Fisher Scientific	Cat #: 15140122
Permount	Fisher Scientific	Cat #: Sp15-500
Picric Acid Solution	Sigma Aldrich	Cat #: P6744
Potassium Bicarbonate	Sigma Aldrich	Cat #: 237205
Potassium Chloride	Fisher Scientific	Cat #: 7447-40-7
Potassium Phosphate, Monobasic	Sigma Aldrich	Cat #: 7778-77-0
Pre-Separation Filters (30 µm)	Miltenyi Biotec	Cat #: 130-041-407
PVDF Membrane	Bio-Rad	Cat #: 1620177
RNase OUT Recombinant Ribonuclear Inhibitor	ThermoFisher	Cat #: 10777019
RNase-Free DNase Set (50)	QIAGEN	Cat #: 79254
SDS	Sigma Aldrich	Cat #: L4509
Sodium Bicarbonate	Fisher Scientific	Cat #: 144-55-8
Sodium Chloride	Fisher Scientific	Cat #: 7647-14-5
Sodium Citrate Tribasic Dihydrate	Sigma Aldrich	Cat #: S4641-500G
Sodium Phosphate, Monobasic, monohydrate, crystal	Fisher Scientific	Cat #: 3818-01
SR-Buprenorphine	ZooPharm	N/A
Sterile Water (Nuclease Free)	ThermoFisher	Cat #: 10977015
SUPERase•In™ RNase Inhibitor (20 U/µL)	Thermo Fisher	Cat #: AM2694
Superfrost plus slide	Fisher Scientific	Cat #: 12-550-15
Surgipro II 8-0MV-135-5 Taper Suture 18"	Covidien/Medtronic	Cat #: VP900x
Tamoxifen	Sigma Aldrich	Cat #: T5648
Tamoxifen Diet (400 TC, 2016, Red)	Harlan Laboratories	Cat #: TD.130860
TAT-Cre	EMD Millipore	Cat #: EG-1001
Taurine	Sigma	Cat #: T8691
TGF-beta 1 Protein R&D Systems Porcine	Fisher Scientific	Cat #: 101B1010
Tissue Tek OCT embedding medium- clear	Fisher Scientific	Cat #: 23-730-571
Triton x-100	Fisher Scientific	Cat #: BP151-100
TRIzol RNA Isolation Reagents	Thermo Scientific	Cat #: 15596018
Trypsin-EDTA 0.25%	Fisher Scientific	Cat #: MT25053CI
Tween-20	Sigma	Cat #: 11332465001
VWR Cell Strainers 70um	VWR	Cat #: 10199-657
X-tremeGENE™ HP DNA Transfection Reagent	Sigma	Cat #: 6366236001
Xylazine	AnaSed	N/A
Xylene	Fisher Scientific	Cat #: X3P-1GAL
Critical commercial assays		
Click-iT™ TUNEL Alexa Fluor™ 647 Imaging Assay, for microscopy & HCS	Fisher	Cat#: C10247
In situ cell death detection kit, TMR red (Roche)	Sigma	Cat #: 12156792910
SuperScript III First-Strand Synthesis System	Life Technologies	Cat #: 18080-051
ITaq Universal SYBR Green	BioRad	Cat #: 1725124

(Continued on next page)

Continued

REAGENT or RESOURCE	SOURCE	IDENTIFIER
Super signal west pico plus chemiluminescent substrate	Thermo Fisher	Cat #: 34580
QIAshredder (250 units)	Qiagen	Cat #: 79656
RNase-Free DNase Set (50)	QIAGEN	Cat #: 79254
RNAqueous Micro Kit	Thermo Fisher	Cat #: AM1931
RNeasy Mini Kit (250)	Qiagen	Cat #: 74106
QuadroMACS™ Separator	Miltenyi Biotec	Cat #: 130-090-976
Trio RNA-Seq	Tecan Genomics, Inc.	Cat #: 0507-32
Chromium Single Cell 3' Library and Gel Bead Kit v.3.1	10x Genomics	Cat #: PN- 2000164
Chromium Single Cell 3' Chip kit v.3.1	10x Genomics	Cat #: PN-120236
Chromium i7 Multiplex Kit	10x Genomics	Cat #: PN- 1000213
Deposited data		
scRNAseq	GEO repository	GSE193308
Experimental models: Cell lines		
Human Cardiac Fibroblasts-Healthy	Promocell	Cat #: C-12375
Human Cardiac Fibroblast-Heart Failure	(Stempien-Otero et al., 2016)	N/A
MBNL1 ^{F/F} Cardiac Fibroblasts	Primary isolation	N/A
MBNL1 ^{F/F} Tcf21 ^{iCre} Cardiac Fibroblasts	Primary isolation	N/A
NTG Cardiac Fibroblasts	Primary isolation	N/A
MBNL1 Tg Tcf21 ^{iCre} Cardiac Fibroblasts	Primary isolation	N/A
Experimental models: Organisms/strains		
B6;B6N- <i>Mbnl1</i> ^{tm1a(EUCOMM)Wtsi}	This Paper	N/A
B6.-Tg(CAG-CAT,- <i>Mbnl1</i>)	(Davis et al., 2015)	N/A
B6.129- <i>Tcf21</i> ^{tm1(cre/Esr1*)Mdt}	(Davis et al., 2015)	N/A
B6.129S- <i>Postn</i> ^{tm2.1(cre/Esr1*)Jmol}	(Kanisicak et al., 2016)	N/A
B6.129(Cg)-Gt(ROSA)26Sortm4 (ACTB-tdTomato,-EGFP)	(Kanisicak et al., 2016; Muzumdar et al., 2007)	N/A
Oligonucleotides		
See Table S1 for all primers	N/A	N/A
Software and algorithms		
FACSDIVA Software	BD Biosciences	N/A
ImageJ	(Schindelin et al., 2012)	https://imagej.net/software/fiji/
Cell Counter Plugin in Fiji	N/A	https://imagej.net/software/fiji/
Veo 2100 Software	Visual Sonics	https://www.visualsonics.com/product/software/vevo-lab
Veo 3100 Software	Visual Sonics	https://www.visualsonics.com/product/software/vevo-lab
GraphPad Prism (v7-8.0)	Graphpad Software	https://www.graphpad.com:443/ RRID:SCR_002798
Cell Ranger	10x Genomics	https://support.10xgenomics.com/single-cell-gene-expression/software/downloads/latest
Seurat	(Butler et al., 2018)	https://satijalab.org/seurat/ RRID:SCR_007322
LASX	Leica	https://www.leica-microsystems.com/products/microscope-software/p/leica-las-x-ls/
IonOptix™ Sarclen Sarcomere Length Acquisition Module	N/A	https://www.ionoptix.com/products/software/sarclen-sarcomere-length-acquisition-module/

(Continued on next page)

Continued

REAGENT or RESOURCE	SOURCE	IDENTIFIER
IonWizard (64-bit) v7.5.1.162	IonOptix	https://www.ionoptix.com/products/software/ionwizard-core-and-analysis/
Galaxy Web Platform	(Afgan et al., 2018)	usegalaxy.org
DESeq2	(Love et al., 2014)	https://bioconductor.org/packages/release/bioc/html/DESeq2.html
HISAT2	(Sirén et al., 2014)	https://daehwankimlab.github.io/hisat2/
g:Profiler	(Raudvere et al., 2019)	https://biit.cs.ut.ee/gprofiler/
Anaconda Python Distribution	N/A	https://www.anaconda.com/products/individual
scipy package	(Virtanen et al., 2020)	https://scipy.org/
scikit-learn package	(Pedregosa et al., 2011)	https://scikit-learn.org/
seaborn package	(Waskom et al., 2020)	https://seaborn.pydata.org/
CurveAlign V4.0 beta	N/A	https://eliceirilab.org/software/curvealign/
R	N/A	https://www.r-project.org
R Studio	N/A	https://www.rstudio.com
ggplot2 package	N/A	https://ggplot2.tidyverse.org
viridis package	N/A	https://cran.r-project.org/web/packages/viridis/index.html
Cell Profiler	N/A	https://cellprofiler.org/

RESOURCE AVAILABILITY**Lead contact**

Further information and requests for resources and reagents should be sent to the lead contact, Jennifer Davis (jendavis@uw.edu).

Materials availability

Reagents used in this study that are not commercially available or obtainable through repositories will be shared upon reasonable request and completion of a material transfer agreement (MTA).

Data and code availability

Single cell RNAseq data have been deposited at Gene Expression Omnibus (GEO) repository and are publicly available now with the accession number GEO: GSE193308.

Any additional information including original western blots, RNAseq, microscopy images, and echocardiography reported in the paper is available through the lead contact upon request.

EXPERIMENTAL MODEL AND SUBJECT DETAILS

Mice were bred and housed at the University of Washington. Rooms have controlled temperature and light/dark cycles with standard chow being provided ad libitum. MBNL1^{Fl} mice were bred to homozygosity with either Tcf21^{iCre} or Postn^{iCre} lines. Both male and female mice of each genotype were used for breeding in all lines. Tamoxifen induction of Cre recombinase expression was started between 6–8 weeks of age and achieved with 5 days of intraperitoneal (IP) injections of pharmaceutical grade tamoxifen dissolved in peanut oil (25mg/kg) followed by 9 additional days on tamoxifen citrate chow (400mg/kg body weight, Harlan Laboratories). Mice remained on Tam chow until the experimental end point unless stated otherwise. Sham or MI surgeries were performed after 2 weeks of Tam treatment, and hearts were harvested for cell or tissue analysis at the indicated time points following surgery. Experimentalists remained blinded to the genotypes until analysis was complete. Both male and female mice were used in all experiments and mice were randomly assigned to groups.

METHOD DETAILS**Animal models**

All animal experimentation was approved by the University of Washington's Institutional Animal Care and Use Committee. Lineage reporter mice were generated by crossing a mouse containing a tamoxifen (Tam)-inducible Cre recombinase cassette knocked into the periostin locus (Postn^{iCre}) with mice containing a membrane targeted dual fluorescent reporter (mT/mG) knocked into the Rosa26

locus (Figure 1G). All cells in Postn^{iCre}-mT/mG mice express membrane-targeted TdTomato (mT) unless Cre is expressed which excises the TdTomato (mT) and moves a membrane-targeted green fluorescent protein (mG) sequence in frame for expression (Kanisicak et al., 2016; Muzumdar et al., 2007). Cardiac fibroblast specific MBNL1 overexpression mice (MBNL1 Tg-Tcf21^{iCre}) were generated by crossing mice containing the human MBNL1 cDNA with mice containing a Tam-inducible *Tcf21-Cre* driver (Figure 2A; Acharya et al., 2011, 2012; Davis et al., 2015). Conditional MBNL1 knockout mice (MBNL1^{F/F}) were generated using targeted C57BL/6 embryonic stem cells (ES) from the International Knockout Mouse Consortium (IKMC). Founders were bred onto a C57BL/6 background and then to mice expressing Flippase to excise the LacZ-neomycin cassettes still present within the floxed MBNL1 allele, as IKMC uses a knockout first approach for their targeted alleles. Once the LacZ-neomycin cassettes were flipped-out, MBNL1^{F/F} mice were crossed with *Tcf21*^{iCre} or Postn^{iCre} to generate cardiac fibroblast and myofibroblast specific MBNL1 knockout mice (Figures 4A and 6A). Tamoxifen induction of Cre recombinase expression was started between 6–8 weeks of age and achieved with 5 days of intraperitoneal (IP) injections of pharmaceutical grade tamoxifen dissolved in 95% peanut oil and 5% ethanol (25mg/kg) followed by 9 additional days on tamoxifen citrate chow (400mg/kg body weight, Harlan Laboratories). Mice remained on Tam chow until the experimental endpoint unless stated otherwise.

Surgical Model of Myocardial Infarction

The surgical model was previously described (Bugg et al., 2020; Molkentin et al., 2017), but briefly 8-week-old mice were anesthetized using injectable ketamine and xylazine. Mice were mechanically ventilated through oral intubation and a lateral thoracotomy was performed to expose the left ventricle. The pericardium was removed, and the left anterior descending artery was permanently ligated more apically to reduce risk of rupture, using 8-0 Surgipro tapered suture. Two days prior to surgery mice were taken off Tam chow for 2 days to prevent any adverse effects of Tam during the surgical procedure and then put back on Tam chow until the studies endpoint. At harvest hearts were excised, rinsed in 1X phosphate buffered saline (PBS), and relaxed in saturated potassium chloride solution before being fixed in formaldehyde and prepped for paraffin or cryo-sectioning. Experimentalists remained blinded to the genotypes until analysis was complete. Both male and female mice were used in all experiments and mice were randomly assigned to groups. Echocardiography was performed on a Vevo2100 or Vevo3100 under isoflurane anesthetic.

In vivo proliferation following MI

Mice underwent MI procedure as stated above. Two boluses of EdU dissolve in PBS (100mg/kg) were injected IP at 24 hours and 9 hours before harvesting. Mice were then euthanized, and hearts fixed in 4% paraformaldehyde overnight. Tissues were then processed through a sucrose gradient (5–30%), embedded in optimal cutting temperature compound (OCT), and prepared for 5μm cryosectioning.

Human primary cardiac fibroblast isolation

Human cardiac fibroblasts were isolated from patients undergoing left ventricular assist device surgery as previously described (Carlson et al., 2017; Farris et al., 2017). Briefly heart samples were rinsed in cold PBS and minced in a 10mL of warm digestion buffer [HBSS, 30mM Taurine, 10mM HEPES, Liberase TH 5mg/mL DNase1 2000U]. The samples are then incubated for 5 minutes, trituated, allowed to gravity settle so the supernatant could be removed, and set off to the side for digestion of remaining tissue. New digestion buffer was added to the remaining tissue, and the process repeated until the tissue was fully digested. Fibroblasts were separated using a Miltenyi MACs magnetic separator positive selection for CD14. Samples were incubated in 1mL of sorting buffer [1XPBS, 0.5%BSA, 2μM EDTA] and 125μL of CD14 microbeads for 1 hour before sorting. Samples were then spun down and stored in TRIzol until RNA isolation. Healthy human fibroblasts were obtained from Promocell.

Mouse primary cardiac fibroblast isolation

Mice were heparinized and cardiac fibroblasts freshly isolated by Langendorff perfusion with type II collagenase (2mg/ml) and Liberase TH (0.4mg/ml) solubilized in Krebs-Henseleit buffer [113mM NaCl, 4.7mM KCl, 0.6mM KH₂PO₄, 0.6mM Na₂HPO₄, 1.2mM MgSO₄·7H₂O, 12μM NaHCO₃, 10μM KHCO₃, 10.8μM Hepes] as previously described (Bugg et al., 2020; Molkentin et al., 2017). For culture experiments cardiac fibroblasts were plated in Dulbecco's Minimal Essential Media (DMEM) with high glucose and supplemented with 1% penicillin and streptomycin (P/S), and 20% fetal bovine serum (FBS) and kept at 37°C with 5% CO₂. Cardiac fibroblasts were expanded to passages 3–5 for experimentation. For some experiments cell-permeant Cre recombinase (TAT-Cre, 1:100, EMD Millipore) was added to the cultures for 2 days to permanently excise MBNL1. For differentiation assays cells were cultured in differentiation media (DMEM + 1% FBS + 1% P/S) with or without recombinant TGFβ (R&D systems, 10 ng/mL) and analyzed 72 hours later by immunofluorescent staining described below. For proliferation assays cardiac fibroblasts were treated with 10μM EdU every 12 hours over 1 day in 2% FBS media. At the studies end point cardiac fibroblasts were fixed in 4% PFA and Click-iT chemistry (Invitrogen) used to detect EdU positivity per the manufacturer's instructions.

In vitro cell treatments

Recombinant TGFβ (10 ng/ml, R&D System) was used to induce myofibroblast transformation. For experiments that used adenoviral gene transfer, cardiac fibroblasts were treated with adenovirus overnight followed by a media change and cells examined 3 days after induction. The following adenoviruses have been previously described: ΔCnA, SRF, GFP, and MBNL1 (Davis et al., 2012, 2015; Liu et al., 2001; Wilkins et al., 2004). An adenovirus expressing GFP was used as a control. Sox9 overexpression was obtained by

transfected cardiac fibroblasts with full length Sox9 cDNA using X-treme Gene transfection reagent (Sigma) diluted in Opti-MEM media at a 4:1 ratio of transfection reagent to plasmid. β gal plasmid was used for control transfections.

Collagen gel contraction assay

Cardiac fibroblasts were isolated, expanded and treated with adenovirus or TGF β 24 hours prior to seeding into collagen gels as previously described (Davis et al., 2012; Ngo et al., 2006). Here 50,000 cardiac fibroblasts were seeded into each gel and then released from the plate into differentiation media (DMEM + 1% FBS + 1% P/S) once they had solidified. Gels were photographed and measured every 12 hours over 4 days. ImageJ software (NIH) was used to calculate the surface area, which are reported as values normalized to the initial size of the gel. Data shown is at 48 hours post seeding.

Transcript stability assay

Tam-treated MBNL1^{Fl/Fl} and MBNL1^{Fl/Fl}-Tcf21^{iCre} cardiac fibroblasts were infected with either AdGFP (controls) or AdMBNL1 for 36 hours at which time transcription was inhibited with 2mg/ml Actinomycin-D (Sigma). RNA was isolated using a Qiagen RNeasy Mini kit from each group after 0, 4, and 8 hours of treatment, reverse transcribed, and analyzed by real-time PCR as previously described (Davis et al., 2015).

Flow cytometry for fibroblast purification

For Postn^{iCre}-mT/mG gene expression and RNA sequencing experiments cardiac fibroblasts were isolated and subjected to flow cytometry as previously described (Molkentin et al., 2017). Briefly cells were strained through a 70 μ m cell strainer and then stained with CD11b (1:50 Miltenyi Biotec 130-113-800) and MEFSK4 (1:50 Miltenyi Biotec 130-120-802) in HBSS with Ca²⁺, Mg²⁺ and 2%FBS. This allows for the removal of contaminating CD11b cells. Cells were then sorted on an Aria II live cell sorter. For Postn^{iCre}-mT/mG experiments the same antibody scheme was used but the MEFSK4⁺ GFP⁻ and MEFSK4⁺ GFP⁺ populations were segregated to compare the populations. RNA isolation was then preformed using an RNaseq Micro Kit which is specifically designed for low RNA yields. Gene specific amplification was used during cDNA synthesis to increase signal of target genes.

Single cell RNA sequencing and analysis

For single cell RNA sequencing, isolated cardiac fibroblasts were subjected to magnetic bead sorting using a Miltenyi QuadroMACS magnetic cell separation kit. Briefly, cells were strained through a 70 μ m cell strainer and resuspended in 180 μ L of sorting buffer (1XPBS, 0.5%BSA, 2 μ M EDTA) and 20 μ L of Cd11b microbeads. Samples were mixed well and incubated for 15 minutes at 4°C. Samples were washed through the magnetic columns and the flow through (containing the Cd11b- fraction) was collected. The cells were spun and resuspend in 160 μ L of sorting buffer with 40 μ L of MEFSK4 (Anti-feeder) microbeads. Cells were again incubated for 15 minutes at 4°C and sorted using magnetic columns. The flow through was discarded, and the magnetic columns containing the MEFSK4+ fraction were removed and rinsed with sorting buffer. Viability was assessed at this point for all preps. Viability was greater than 90% for all samples. Cells were lysed as previously described (Alexanian et al., 2021). Briefly cells were spun and rinsed in 1x HBSS with no FBS. Pellets were resuspended in 200 μ L of Lysis buffer (Tris-HCl 10mM pH 7.4, NaCl 10mM, MgCl2 3mM, Tween-20 0.1%, NP40 0.1%, Digitonin 0.01%, in Nuclease-free water), pipetted 10 times and kept on ice for 5 minutes. Nuclei were washed with 1 mL of wash buffer [Tris-HCl 10mM pH 7.4, NaCl 10mM, MgCl2 3mM, Tween-20 0.1%, in Nuclease-free water], inverting 3 times to mix. Nuclei were spun at 5000g for 3 minutes at 4°C. Nuclei were further washed in 1.2mL of 1X PBS with 1%BSA and filtered through a 30 μ m filter to remove any debris. Nuclei were counted using Trypan blue and a hemocytometer. Nuclei were resuspended at a concentration of 1000nuclei/ μ L in 1XPBS with 8300 nuclei being loaded for subsequent 10X Genomics Chromium single cell RNAseq preparation.

Single cell droplet libraries were generated in the 10X Genomics Chromium controller according to the manufacturer's instructions in the Chromium Single Cell 3' Reagent Kit v.3.1 with Dual Indexing. Additional components used for library preparation include the Chromium Single Cell 3' Library and Gel Bead Kit v.3.1 (PN- 2000164) and the Chromium Single Cell 3' Chip kit v.3.1 (PN-120236). Libraries were prepared according to the manufacturer's instructions using the Chromium Single Cell 3' Library and Gel Bead Kit v.3.1 (PN- 2000164) and Chromium i7 Multiplex Kit (PN- 1000213). Final libraries were sequenced on the NextSeq 2000. All 14 samples were pooled and sequenced in one single lane. Sequencing parameters were selected according to the Chromium Single Cell v.3.1 specifications. Libraries were sequenced to a mean read depth of at least 20,000 total aligned reads per cell.

The Cell Ranger Single-Cell Software Suit (Zheng et al., 2017) was used to perform sample demultiplexing, barcode processing and single-cell 3' gene counting. For each sample, reads were aligned to the Mouse (mm10) 2020-A premRNA reference genome using CellRanger count v6.1.1. CellRanger Aggr (v6.1.1) was used to aggregate count matrices across samples with normalize=none. Only confidently mapped reads with valid barcodes and unique molecular identifiers were used to generate the gene-barcode matrix. Further analyses for quality filtering was performed using the Seurat R package (Butler et al., 2018). We calculated the distribution of detected genes per cell and removed cells in the top 1% quantile or those which had fewer than 200 detected genes. Cells were removed with more than 15% of the transcripts coming from mitochondrial genes. After quality filtering, reads were normalized to account for technical variation in the dataset including sequencing depth. To do this, we implemented the SCTransform function (Hafemeister and Satija, 2019) with the "glmGamPoi" method (Ahmann-Eltez and Huber, 2021); mitochondrial mapping percentage was also regressed out using the vars.to.regress argument. Principal component analysis was performed on the scaled data, and then cells were clustered on the first 18 principal components using the FindNeighbors function and the FindClusters function with resolution 0.5.

To visualize the data, we used non-linear dimensional reduction via Uniform Manifold Approximation and Projection (UMAP) to project cells in 2D space on the basis of the first 18 principal components (McInnes et al., 2018). Nine fibroblast clusters were identified based on expression of *Col1a1*, *Pdgfra*, and *Postn*, and seven clusters expressing markers of non-fibroblast populations, which likely represent contaminating non-fibroblast nuclei after fibroblast isolation. These non-fibroblast clusters were removed, and the clustering processes were repeated resulting in the identification of 13 fibroblast subpopulations. In total, we analyzed 20814 fibroblast nuclei (5302:NTG-SHAM, 5611:NTG-MI, 1831: MBNL1^{F/F}-Tcf21^{iCre} -SHAM, 3163: MBNL1^{F/F}-Tcf21^{iCre} -MI, 2495: MBNL1 Tg-Tcf21^{iCre}-SHAM, 2412: MBNL1 Tg-Tcf21^{iCre} -MI) with a median of 2875.5 UMI per cell and 1322 unique genes per cell. Cluster markers were identified using the FindMarkers function with a Wilcoxon rank sum test; cell type identities were assigned to clusters by examination of top cluster markers, differential expression analysis between individual clusters, and consultation of previous single cell RNA sequencing datasets of isolated fibroblasts. Differential expression analysis between populations was completed using the FindMarkers function with the Wilcoxon rank sum test based on genes which were expressed in at least 10% of cells for at least one of the populations being compared and with an absolute log₂ fold change greater than 0.25. Over-representation of GO terms in gene lists was calculated using the goset function in the Gprofiler (Kolberg et al., 2020) R package. We also performed pseudotime analysis using Monocle3 (Qiu et al., 2017; Trapnell et al., 2014) with the SeuratWrappers package as described in the tutorials (Stuart and Srivastava, 2021). Our Seurat object was converted into a CellDataSet object using the as.cell_data_set() function. Pseudotime estimates were calculated with the order_cells function with root nodes selected in the F-SH2 and F-EPI populations. Pseudotime values were then extracted and added to our Seurat object. Single cell RNAseq data have been deposited at Gene Expression Omnibus (GEO) repository with the accession number GSE193308.

Cardiomyocyte isolation

Mouse ventricular myocytes were freshly isolated by Langendorff perfusion with Liberase TM (0.225 mg/mL, Roche) in Krebs-Henzeleit buffer (135mM NaCl, 4.7mM KCl, 0.6mM KH₂PO₄, 0.6mM Na₂HPO₄, 1.2mM MgSO₄, 20mM Hepes, 10μM BDM, and 30mM Taurine) as previously described (Hegyi et al., 2020). Ventricular myocytes were dispersed mechanically and filtered through a 200μm nylon mesh then allowed to sediment for ~10 minutes. The sedimentation was repeated three times using increasing [Ca²⁺] from 0.125 to 0.25 then 0.5 mmol/L. Myocytes were plated on laminin coated coverslips in Tyrodes solution (137mM NaCl, 5.4mM KCl, 0.5mM MgCl₂, 1.2mM CaCl₂*2H₂O, 10mM Hepes, and 5mM Glucose, 7.4 pH) for 1 hour prior to functional measurements or relaxed in 25μM blebbistatin and fixed with 4%PFA at room temperature for 15 minutes.

Myocyte morphology tracing

Myocytes were stained with a dilution of 1:100 Wheat Germ Agglutinin, Alexa Fluor™ 488 Conjugate (W11261) for 1 hour at room temperature. 40 cells per mouse were manually traced using Fiji.

Measurements of myocyte contractility

Sarcomere measurements were obtained from isolated myocytes using the IonOptix™ SarcLen Sarcomere Length Acquisition Module with a MyoCam-S3 digital camera (Ionoptix Co., Milton, MA) attached to an Olympus uWD 40 inverted microscope. For these measurements myocytes were bathed in 1.2mM Ca²⁺ Tyrode's buffer (137mM NaCl, 5.4mM KCl, 0.5mM MgCl₂, 1.2mM CaCl₂*2H₂O, 10mM HEPES, 5mM Glucose, 7.4 pH) and kept at 37°C. To jumpstart pacing, myocytes were stimulated with frequencies varying from 0.5, 1.0, and 1.5 Hz at 10V for a minimum of 10 contractions at each frequency. Sarcomere lengths were then measured in real time at a frequency of 0.5Hz and averaged across 10-15 contraction cycles. Blinded analysis was performed using the IonWizard software. Statistical analyses were performed on individual myocyte measurements (n ~ 30 myocytes/mouse; n=3). Significance was determined using Student's t-test.

Gene expression analysis

Real time polymerase chain reaction (RT-PCR) methods are previously described from our laboratory (Bugg et al., 2020; Davis et al., 2012, 2015; Molkentin et al., 2017). Briefly, total RNA was extracted using RNAqueous Micro Kit for all flow sorted samples or using QIA shredder homogenization and the Qiagen RNeasy kit for in vitro culture. Total RNA was reverse transcribed into cDNA using random hexamer primers and SuperScript III first-strand synthesis kit (Invitrogen) according to the manufacturer's instructions. RT-PCR was performed on a CFX96 Real-Time System with a Biorad C1000 Touch Thermal Cycler using Sso Advanced SYBR Green (Biorad). Thermocycler conditions were as follows: Polymerase Activation and DNA Denaturation at 95°C for 30s, Denaturation at 95°C for 5s, Annealing/Extension and Plate Read at 56°C for 30s. 39 cycles of denaturation and annealing were performed. Fold changed in gene expression was determined using the 2^{ΔΔCT} method. Any differences in cDNA were correct by calculating the difference (ΔCT) between the target gene's threshold cycle (CT) and the CT for 18s, which serves as the housekeeping gene. Primer list can be found in Table S1.

Bulk RNA Sequencing (RNAseq)

FACs sorted cell pellets were snap frozen and stored at -80°C until all samples were collected. Total RNA was extracted using RNAqueous Micro Kit and RNA libraries were generated using a Tecan Trio library prep kit, using 2ng of total RNA following manufacturers protocol. 4 PCR cycles were run for full length cDNA amplification. Libraries were pooled and sequenced through an external provider. Cleaned RNAseq reads were uploaded to the public Galaxy server at usegalaxy.org for bioinformatic analysis (Afgan et al.,

2018). Reads were aligned using HISAT2 to the mm10 reference genome, summarized using featurecounts, and differential expression between timepoints and genotypes were tested using DESeq2 (Kim et al., 2019; Liao et al., 2014; Love et al., 2014). Genes with an adjusted $p < 0.05$ were considered significantly differentially expressed. PCA was performed on the \log_2 normalized counts matrix from DESeq2 using the scikit-learn package (Pedregosa et al., 2011). Heatmaps and gene expression scatterplots were generated from the \log_2 normalized counts output from DESeq2 using the seaborn package in Python (Waskom et al., 2020). Functional enrichment analysis was conducted using the GProfiler web app, inputting all significant differentially expressed genes as an ordered query (Raudvere et al., 2019). To assess time course expression of clustered, a pairwise correlation matrix between time course-significant genes was calculated, hierarchically clustered using the scipy package in Python, and plotted with seaborn (Virtanen et al., 2020; Waskom et al., 2020). Functional enrichment analysis on genes from each cluster was performed using GProfiler, and \log_2 normalized gene expression levels per cluster were calculated and plotted over time using seaborn (Raudvere et al., 2019).

Western blot

Tam-induced MBNL1^{F/F} and MBNL1^{F/F}-Tcf21^{iCre} fibroblasts treated with 10ng/ml TGF β and cell lysates were collected 48 hours later in RIPA buffer [5 M NaCl, 10% Triton-X 100, 25%SDS, 1 M Tris-Cl PH 7.4]. Lysates were diluted in Laemmli buffer with DTT, 20 μ g of protein was loaded into 10% SDS-PAGE acrylamide gels and transferred to PVDF membrane for immunodetection. MBNL1 was detected with anti-MBNL1 (1:100, rabbit polyclonal antibody, Abcam) overnight at 4°C with goat anti-rabbit HRP conjugate secondary at 1:10,000 from EMD Millipore for 1 hour. Anti-GAPDH (1:10,000, mouse monoclonal, Fitzgerald Industries) overnight at 4°C with goat anti-mouse HRP conjugate at 1:10,000 from EMD Millipore for 1 hour was used as a loading control.

Histology and immunohistochemistry

Hearts were cut in half on the transverse plane prior to processing and sectioning. 5 μ m paraffin sections were obtained for Sirius Red/Fast Green staining (0.1% Direct Red 80, 0.1% Fast Green in Picric Acid). This method stains muscle tissue in green and fibrotic scar in red. Images of whole hearts were taken at 2x magnification and quantified in ImageJ using color thresholding. Serial sections were then used for α SMA (1:500 Sigma) and IsolectinB4 (IB4) (10ug/mL Vector Biolabs) staining to quantify myofibroblast number in paraffin. Sox9 (1:500, Millipore) and PDGFR α (1:100 R&D systems) staining was done on independent OCT samples. Collagen 3a1 (1:250 Santa Cruz) and Collagen 5a1 (1:250 Santa Cruz) were stained on serial OCT sections. Slug (1:100, Santacruz), Tbx18 (1:500, Santacruz), and Wt-1 (1:1000, Santacruz) were co-stained with PDGFR α (1:100 R&D systems) in OCT sections. These methods are previously described from our laboratory. Here sections were deparaffinized (or in the case of OCT sections they were just rinsed in 1XPBS) and the blocked in PBS with 1% BSA and 0.1% cold fish skin gelatin. Primary antibodies were incubated overnight in blocking solution at 4°C (Bugg et al., 2020; Molkentin et al., 2017). AlexaFluor secondary antibodies (1:1000 Invitrogen) were used for 1.5 hours at room temperature to detect the antigen. Hoechst (1:2000 Thermo Fisher) was used to visualize Nuclei. Additional groups were incubated in primary or secondary antibody alone to control for non-specific signaling for imaging analysis. To visualize EdU staining in vivo Click-iT chemistry was used following the manufactures instructions with the substitution of normal horse serum (NHS) for PDGFR α (1:100 R&D systems) co-staining. To visualize cellular death, serial sections were stained using the Roche In Situ Cell Death Detection Kit (TMR red, Roche 12156792910) according to manufacturer's recommendations. To permeabilize the samples prior to TUNEL labeling, slides were incubated with 1X Biogenex Antigen-Retrieval Solution for 15 min at 80°C and 0.1% Triton, 0.1% Sodium Citrate Tribasic dihydrate for 8 min at room temperature. Following TUNEL labeling, slides were blocked in PBS containing 2% BSA, 2% Normal Goat Serum (NGS), 0.1% NP40 and co-stained with Hoechst and α -Actinin (1:200 Sigma-Aldrich) or PDGFR α (1:100 R&D Systems) to assess myocyte or fibroblast-specific cell death. Wash steps were performed with PBS containing 0.5% Triton. All samples were mounted using Mowiol 4-88.

Immunocytochemistry

Immunofluorescence staining procedures followed previously described methods (Bugg et al., 2020; Molkentin et al., 2017). Briefly, cardiac fibroblasts were fixed in 4% paraformaldehyde, permeabilization in 1X PBS containing 0.1% Triton-X100, and blocked in PBS containing 0.1% Triton-X100 and 10% Normal Goat Serum (NGS). Primary antibody for α SMA (1:500 Sigma) was incubated at room temperature for 2 hours. AlexaFluor secondary antibodies (1:1000 Invitrogen) were used for 1.5 hours at room temperature to detect the antigen. Hoechst was added with secondary antibody used to visualize nuclei. Additional groups were incubated in primary or secondary antibody alone to control for non-specific signaling for imaging analysis. Samples were mounted using Mowiol 4-88.

Image analysis

To quantify α SMA $^+$ or EdU $^+$ fibroblasts *in vitro*, cells were manually counted across 10 representative fields of view (FOVs) and normalized to the total number of nuclei to get a percent of total population. To score the number of α SMA $^+$ myofibroblasts in baseline MBNL1 Tg-Tcf21^{iCre} mice and NTG-Tcf21^{iCre} control hearts, the entire cross section of a heart was imaged and the total number of α SMA $^+$ IB4 $^-$ cells were manually scored. Since there are so few cells in these hearts they are shown as raw values and not normalized to fibroblast number or heart area. For infarcted tissue 9-16 FOV of the infarct and border zone were imaged and the number of α SMA $^+$ IB4 $^-$ cells were scored and then normalized to the average number of cells per FOV. This same technique was used for Sox9 $^+$ PDGFR α $^+$ analysis. For *in vivo* proliferation quantification we first scored for the total number of PDGFR α $^+$ fibroblasts in the infarct and border zone using the Cell Counter Plugin in Fiji (NIH). Then the Click-iT staining was overlaid with the PDGFR α signal, and we scored for the number of

PDGFR α^+ EdU $^+$ allowing us to calculate the percent of the total fibroblast population that was proliferating. To quantify cell death, three FOV images were taken in the infarct regions and number of TUNEL $^+/\alpha$ -Actinin $^+$ and TUNEL $^+/\text{PDGFR}\alpha^+$ nuclei were counted. These values were compared to overall number of TUNEL $^+$ nuclei to achieve percent myocyte and fibroblast death in the infarct zones. Collagen 3a1 and 5a1 intensity was measured across the infarct using cell profiler and intensity was normalized to overall Hoechst intensity.

Analysis of collagen birefringence

Images of the left ventricular infarct zone were taken at 40x magnification with 3 FOV imaged per mouse. Filters were used to reduce the amount of bright light and the polarizer was rotated to 90 degrees. This produced images with a very black background and bright collagen birefringence. Analysis of collagen birefringence was completed using HSB color thresholding in Fiji (Hue categories: Red/White 2-235 without pass, Red/Orange 3-21, Yellow/Green 24-120). The percent area of each color category was then normalized to the total fiber area from Hue 120-235 without pass.

RNA immunoprecipitation in cardiac fibroblasts

Cardiac fibroblasts were isolated as stated above. Cells were passaged twice and treated with AdMBNL1 (MOI=500) for 48 hours. Fibroblasts were scraped in cold 1X PBS and pelleted by centrifugation for 3 minutes at 1000 rpm. Cells were then lysed in RIP buffer [150mM KCl, 25mM Tris-HCl pH 7.4, 5mM EDTA, 0.5% NP-40, 0.5mM DTT, 100U/mL RNase OUT Recombinant Ribonuclease Inhibitor (ThermoFisher 10777019), and 1X complete EDTA-free Protease Inhibitor Cocktail (Sigma 11836170001)]. Lysates were mechanically sheared by Dounce homogenization using 18 strokes. Nuclear membrane and debris were pelleted by centrifugation at 13000 rpm for 10 minutes at 4°C. For each IP, 10% of the input lysate was placed directly into Trizol; lysates were then incubated overnight with 5 μ g of either Rabbit anti-FLAG (Sigma F7425) or Rabbit IgG Isotype control (Cell Signaling 3900S) antibody at 4°C with gentle rotation. Following overnight incubation, 40 μ l of Dynabeads Protein A (ThermoFisher 10001D) were washed 6x in RIP buffer and then added to RIP lysates for 1 hour at 4°C with gentle rotation. Beads and bound material were collected using a DynaMag magnet, and the beads were washed 6x in RIP buffer and 1x in 1x PBS containing 0.5mM DTT, 100U/mL RNase OUT, and 1x complete EDTA-free Protease Inhibitor Cocktail. Following washing, Trizol was added to isolate bound RNA. Following RNA isolation and cDNA conversion, *Cdkn1a*, *Sox9* and *Fstl1* transcripts were quantified by qPCR and analyzed using the percent input method.

Decellularization and collagen alignment analysis

Hearts were excised and retrograde perfused briefly with 1X phosphate buffered saline (PBS), then perfusion decellularized for 12 hours with a 1% aqueous solution of SDS, followed by a 1 hour wash of 1% Triton-X 100 to remove residual SDS. Hearts were then washed extensively in deionized H₂O and mounted in a 1% wt/vol agarose hydrogel for imaging. Second harmonic images were obtained on an Olympus FV1000MP multiphoton microscope with 860nm excitation (MaiTai DeepSee HP, 59% power) and 420-460nm emission. Z-stacks of 20 images with 1.8 μ m spacing were obtained at 25x magnification and 2.0 zoom in the border and infarct regions, then converted to maximum intensity projections in ImageJ 2.3.0 (Rueden et al., 2017; Schindelin et al., 2012). Fiber metrics were quantified using CurveAlign 4.0 using the CT-Fire Fibers mode and default parameters (Liu et al., 2017).

QUANTIFICATION AND STATISTICAL ANALYSIS

Time course plots (Figures 1C–1E) were generated with 95% confidence intervals using the pointplot function in seaborn (Waskom et al., 2020). Prism versions 7 and 8 were used for plotting all other data and statistical analysis. Data are represented as mean \pm SEM. 2-way ANOVA with Tukey post hoc analysis was used for multiple comparisons. Two-tailed t-tests were used for pairwise comparisons with a p < 0.05 considered significant.